Self-reductive synthesis of MXene/Na$_{0.55}$Mn$_{1.4}$Ti$_{0.6}$O$_4$ hybrids for high-performance symmetric lithium ion batteries.

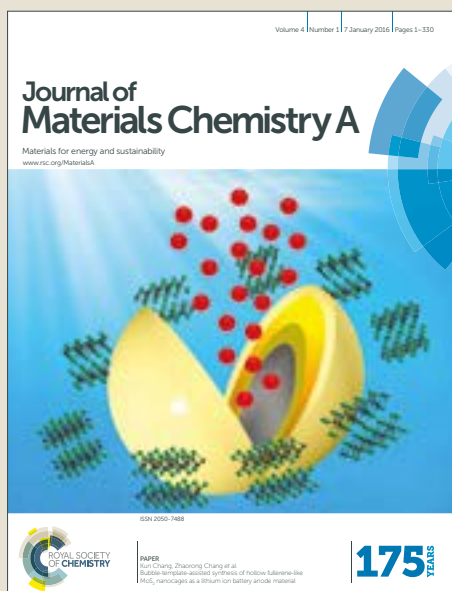ZOU, G., GE, B., ZHANG, H., ZHANG, Q., FERNANDEZ, C., LI, W., HUANG, J. and PENG, Q.

2019

Journal of
Materials Chemistry A

Accepted Manuscript

Volume 4 | Number 1 | 7 January 2016 | Pages 1–330

Journal of
Materials Chemistry A

Materials for energy and sustainability
www.rsc.org/MaterialsA

ISSN 2050-7488

ROYAL SOCIETY OF CHEMISTRY

PAPER
Kun Chang, Zhaorong Chang et al.
Bubble-template-assisted synthesis of hollow fullerene-like
MoS₂ nanocages as a lithium ion battery anode material

175 YEARS

This is an Accepted Manuscript, which has been through the Royal Society of Chemistry peer review process and has been accepted for publication.

Accepted Manuscripts are published online shortly after acceptance, before technical editing, formatting and proof reading. Using this free service, authors can make their results available to the community, in citable form, before we publish the edited article. We will replace this Accepted Manuscript with the edited and formatted Advance Article as soon as it is available.

You can find more information about Accepted Manuscripts in the author guidelines.

Please note that technical editing may introduce minor changes to the text and/or graphics, which may alter content. The journal's standard Terms & Conditions and the ethical guidelines, outlined in our author and reviewer resource centre, still apply. In no event shall the Royal Society of Chemistry be held responsible for any errors or omissions in this Accepted Manuscript or any consequences arising from the use of any information it contains.

ROYAL SOCIETY
OF CHEMISTRY

rsc.li/materials-a

Journal of Materials Chemistry A

PAPER

Self-reductive synthesis of MXene/Na$_{0.55}$Mn$_{1.4}$Ti$_{0.6}$O$_4$ hybrids for high-performance symmetric lithium ion batteries

Guodong Zou[a], Bingcheng Ge[a], Hao Zhang[a], Qingrui Zhang[b], Carlos Fernandez[c], Wen Li[d], Jianyu Huang[a] and Qiuming Peng*[a]

Increasing environmental problems and energy challenges have attracted urgent demand for developing green and efficient energy-storage systems. The search for new materials that could improve the performance of Li-ion batteries (LIBs) is one of today's most challenging issues. Herein, a stable symmetric LIB based on the bipolar material-MXene/Na$_{0.55}$Mn$_{1.4}$Ti$_{0.6}$O$_4$ is developed. This bipolar hybrid material shows a typical MXene-type layered structure with high conductivity, containing two electrochemically active redox couples of Mn^{4+}/Mn^{3+} (3.06 V) and Mn^{2+}/Mn (0.25 V), respectively. This MXene/Na$_{0.55}$Mn$_2$O$_4$-based symmetric full cell exhibits the highest energy density of 393.4 Wh kg^{-1} among all symmetric full cells reported so far, wherein it bestows a high average voltage of 2.81 V and a reversible capacity of 140 mAh g^{-1} at a current density of 100 mA g^{-1}. In addition, it offers a 79.4% capacity retention after 200 cycles at a current density of 500 mA g^{-1}. This full symmetric lithium ion battery will stimulate further research on new LIBs using the same active materials with improved safety, low cost and long life-span.

Introduction

Among various energy-storage technologies, commercialized LIBs are playing very important roles in the portable electronic devices or the next-generation electric vehicles. However, owing to some intrinsic disadvantages of the employed electrodes, such as high safety risk, limited life span, sophisticated production process and high cost, the practical utilization of these systems is still limited.[1] Among these developing strategies, the symmetric electrodes is deemed as an alternative to improve the overall performance of LIBs. Symmetric electrodes are two identical electrodes that can be employed as both cathode and anode in an individual energy-storage system.[2] Compared with other batteries, the symmetric batteries offer three main advantages. Firstly, the batteries may be overcharged to some extent and can buffer the large volume expansion (cathode expansion accompanied by anode shrinkage) more effectively due to a unique configuration.[3] Secondly, symmetric electrodes may eliminate the possibility of side reactions between the electrolyte and the lithium foil. Those side reactions could be restricted if the same electrolyte is used in a full cell, improving the safety and

cyclability.[4] Finally, the manufacturing costs and the fabrication process can be greatly reduced and simplified in terms of industrial applications. In addition, the processing cost of the electrode coating can be reduced, as only one type of the electrode needs to be produced, which makes it more attractive for the scalable production.[5] Consequently, the research for finding new symmetric electrode materials with low cost, improved safety, and high-energy density has been an important trajectory to satisfy the ever-growing energy demands.

Theoretically, the transition elements with various valences which are potential to form two redox couples are promising for symmetric cells. However, owing to the structural instability and poor conductivity, the very limited transitional couples have been achieved as symmetric electrodes. Among the symmetric electrodes for LIBs reported so far, it mainly involves three species: phosphate salt-based (LiV$_P$O$_4$F[6], Li$_3$V$_2$(PO$_4$)$_3$[7]), titanate salt based (Li$_{4/3}$Ti$_{5/3}$O$_4$[8]) and vanadate salt-based (Na$_{1.16}$V$_3$O$_8$[9]). Unfortunately, compared with the commercial full LIBs, there are still shortcomings on these symmetric LIBs, such as low energy density, high cost, poor conductivity, structural instability and narrow output potential.[10] As a result, some new systems are desirable for the development of new symmetric LIBs.

Birnessite, one of the polymorphs of manganese oxides, has a good layered structure consisting of edge-sharing MnO$_6$ octahedra with water molecules in the interlayer space with intercalated cations, such as K$^+$ and Na$^+$.[11] Thus, it provides more favourable pathways for lithium intercalation and deintercalation as compared with monoclinic oxides. However, its potential applications in practical LIBs are still limited due to

a. State Key Laboratory of Metastable Materials Science and Technology, Yanshan University, Qinhuangdao 066004, China. E-mail: pengqiuming@ysu.edu.cn
b. Hebei Key Laboratory of Applied Chemistry, School of Environmental and Chemical Engineering, Yanshan University, Qinhuangdao 066004, China.
c. School of Pharmacy and Life Sciences, Robert Gordon University, Aberdeen, AB107GJ, UK.
d. Institute of Energy Resources, Hebei Academy of Sciences, Shijiazhuang, 050081, China.
† Electronic Supplementary Information (ESI) available: Additional details and supplementary results. See DOI: 10.1039/x0xx00000x

This journal is © The Royal Society of Chemistry 2019

J.Mater. Chem. A, 2019, **00**, 1-3 | **1**

its poor electrical conductivity, large volume expansion during repeated charge/discharge cycling processes and complex synthesis process.[12,13] It is still a challenge to prepare high conductivity and fine birnessite materials hitherto.[10,12]

Herein, we firstly achieved a new MXene/ $Na_{0.55}Mn_{1.4}Ti_{0.6}O_4$ (denoted as MXene/NMTO) hybrid by means of self-reduction of MXene ($Ti_3C_2(OH_xF_{1-x})_2$). The fine $Na_{0.55}Mn_{1.4}Ti_{0.6}O_4$ has been homogenously distributed on the surface of MXene under microwave-assisted reaction, and thus this hybrid remained as its two dimensional MXene-type structure. The MXene acted as both reductant and substrate during the reaction process. The MXene/NMTO hybrid forms a unique bipolar electrode materials with a high cycling stability, a remarkable high average voltage of 3.06 V *vs* Li⁺/Li in the cathode side and a very safe potential of 0.25 V at the anode side. The symmetric lithium full cells based on this bipolar material show the highest energy density of 393.4 Wh kg⁻¹ among all symmetric LIBs and NIBs reported so far, a high average voltage of 2.81 V, a reversible discharge capacity of 140 mAh g¹ at a current density of 100 mA g⁻¹, and a 79.4% capacity retention after 200 cycles at a current density of 500 mA g⁻¹. The work will provide new avenues for designing advanced electrode materials for new symmetric LIBs.

Experimental procedure

Synthesis of samples

All the reagents obtained from Aladdin (shanghai, china) were of analytical grade and used without any further purification after purchase in the present study. MXene was synthesized as previously reported in our work.[14-15] 0.3 g MXene was added to 40 ml deionized water and vigorously stirred for 30 min. The dispersion was sonicated for 30 min to get a uniform suspension. Then, 1 ml 40 wt% $NaMnO_4$ aqueous solution was added dropwise in the above solution under stirring. After 10 min vigorous stirring, the mixed solution was conducted on a microwave system (MS, XH-8000, Beijing XiangHu Science and Technology Development Co., Ltd., China) equipped with in-situ magnetic stirring and heated at 110°C for 15 min to prepare MXene/NMTO hybrids. After the reaction, the suspension was centrifuged and rinsed three times using deionized water and ethanol, and freeze-dried under vacuum for 12 hours on a freeze-dryer (FD-1A-80, Beijing Boyikang Laboratory Instrument Co. Ltd.). For comparison, neat $Na_{0.55}Mn_{1.4}Ti_{0.6}O_4$ (NMTO) sample was produced by microwave reaction at 150 °C for 15 min following the same procedure.

Material characterization

The phase purity and crystal structure of the samples were recorded on X-ray diffraction (Rigaku D/MAX-2005/PC) using Cu Kα radiation (λ=1.5406 Å) with a step scan of 0.02° per step and a scan rate of 4°/min from 5° to 70°. The microscopic features of the samples were characterized by a FESEM (Hitachi S4800) and TEM (a Titan ETEM G2) using an accelerating voltage of 300 kV. An EDX analyzer mounted on the Hitachi S4800 and EELS mounted on Titan ETEM G2 were

used to collect the elemental compositions of the products. Inductively coupled plasma (ICP, ICAP 6300 Thermo Scientific, USA) was conducted to analyse the elemental contents. An H7756 four-point probe was used to measure the electrical conductivity of different samples. The specific surface areas and pore sizes were measured by a Micrometrics ASAP2020 using nitrogen gas adsorption at 77 K. The surface elemental analysis of the samples were conducted on the XPS (ThermoFisher K-Alpha) using monochromatic Al Kα (1486.71 eV) X-ray radiation (15 kV and 10 mA).

Electrochemical measurements

Electrochemical performance tests were carried out using a coin-type 2025 cells with lithium metal as the counter and reference electrode. The working electrodes were made of 80 wt% of active material, 10 wt.% acetylene black and 10 wt% of polyvinylidene fluoride in methyl-2-pyrrolidone. After mixing thoroughly, the slurries were casted on battery grade copper foils for the anode and aluminium foils for the cathode. Then, the electrodes were dried in a vacuum oven at 80°C for 12h. The loading amount of each electrode was 1.0-1.5 mg/cm⁻² and electrodes were punched as 12 mm discs. All the electrodes were assembled in an argon-filled glove box with concentrations of moisture and oxygen below 1 ppm. A polypropylene membrane (Celgard 2400) and 1.0 M $LiPF_6$ in the mixture of ethylene carbonate /dimethyl carbonate /ethylmethyl carbonate (1:1:1 by volume) were used as the separator and electrolyte, respectively. A Land Battery Measurement system (Land CT2001A, China) was applied to test galvanostatic charge-discharge cycles at different rates with a voltage window of 0.01-3 V for the anode and 1.5-4.8 V for the cathode. The CV was performed on an electrochemical workstation (Bio-logic, VSP) with a scan rate of 0.2 mV/s. Electrochemical impedance spectroscopy (EIS) was measured by an electrochemical workstation (Bio-logic, VSP) in the frequency ranged from 100 kHz to 100 mHz, with an amplitude of the alternating voltage of 5 mV. Before the lithium ion full cells fabrication (the MXene/NMTO hybrids were used as both anode and cathode), the MXene/NMTO anode and the MXene/NMTO cathode were pre-lithiated and pre-delithiated for the first cycle activation. Then, pre-delithiated MXene/NMTO cathode was reassembled with the pre-lithiated MXene/NMTO anode to constitute a full cell using the identical assembly process as the half cell. The mass ratio of cathode/anode was 4.0-4.2. The full cell was measured over the voltage range of 0.6-3.7 V.

In situ TEM test

The ETEM (G2-FEI) was used to observe the *in situ* TEM of nano-battery system. The pure $Na_{0.55}Mn_{1.4}Ti_{0.6}O_4$ sample attached to an aluminium rod was served as the working electrode, and lithium scratched on the tungsten tip was regarded as the reference and counter electrode. The *in situ* nano-battery reaction process was controlled by changing a bias voltage from -6 to 6 V.

Results and discussion

Characteristics of heterogeneous hybrids

A two-step reaction process is illustrated in Scheme 1. The first step involved the preparation of MXene precursor. Typically, as we previously reported,[14,15] the Ti_3AlC_2 powders were added into a mixture of HF solution to remove the Al layer. After etching, the resultant sediments were separated and dried to attain MXene precursor. Secondly, a simple microwave-assisted reaction containing $NaMnO_4$ solution (the detailed procedure is described in the Experimental procedure) has been performed to prepare heterogeneous hybrids. The exfoliated MXene precursor has been identified by X-ray diffraction (XRD, Fig. 1a) and field emission scanning electron microscopy (FESEM, Fig. S1, ESI†). The (001) peak at about 9º confirms that the sheets comprise of MXene layers containing OH and F groups.[16] The gap width is ~ 120±30 nm and the layer thickness is ~20 nm, respectively. The layer spacing is ~ 0.987 nm. The structure is consistent with that reported previously.[17,18] In contrast, the sample surface is covered by a thin crystalline film after $NaMnO_4$ microwave-assisted reaction followed by dried treatment, confirmed by FESEM (Fig. 1b-c) and transmission electron microscopy (TEM, Fig. 1d). The thickness is ~45 nm (Fig. 1e). The surface elemental composition contains Na, Mn, O, Ti and C as revealed by dispersive X-ray spectroscopy (EDX, Fig. S2, ESI†). The low-loss and core-loss of electron energy loss spectroscopy (EELS, Fig. 1f-g) demonstrate that the MXene sample is mainly composed of Ti (48.5 and 456 eV), and C (23.8 and 283 eV), while the MXene/NMTO sample contains some Na (31 eV), Mn (81 and 637 eV) and O (532 eV) except for Ti and C peaks. The ICP and EDX (Table S1 and S2, ESI†) results of the NMTO sample confirm the composition of $Na_{0.55}Mn_{1.4}Ti_{0.6}O_4$, which shows a similar crystal structure of $Na_{0.55}Mn_2O_4$ (JCPDF No. 43-1456) (Fig. 1a). The high resolution TEM (HRTEM, Fig. 1h) images show that the lattice spacings of the surface layers are 0.252 and 0.248 nm, respectively, which match the (110) and (200) planes of Ti-doped $Na_{0.55}Mn_2O_4$ phase, respectively. The concentration of the $Na_{0.55}Mn_{1.4}Ti_{0.6}O_4$ in MXene/NMTO sample is ~ 66 wt.% based on both the

inductively coupled plasma (ICP, Table S1, ESI†) and the EDX results (Table S2, ESI†). The number of crystalline H_2O is ~1.5 in $Na_{0.55}Mn_{1.4}Ti_{0.6}O_4$ compound as revealed by the thermo-gravimetric analysis (TG, Fig. S3a-b, ESI†). The XRD patterns after heat treatment under different temperatures (Fig. S3c, ESI†) reveal that the water molecules are typically intermolecular. Therefore, this new hybrid is composed of MXene and $Na_{0.55}Mn_{1.4}Ti_{0.6}O_4·1.5H_2O$ (Fig. 1), and it can be denoted as MXene/NMTO.

To understand the formation process of this hybrid, the morphology evolution is monitored at different reaction times and temperatures. The initial reaction occurred at 110 ºC (5 min), in which the surface became coarse, with the formation of irregularly sized particles (Fig. S4, ESI†), indicating that the surface region of MXene was covered by NMTO. With increasing incubation time (30 min), the thickness of the MXene layer became thinner, and the amount of NMTO increased correspondingly. The primitive MXene layer has absolutely disappeared after reacting for 45 min. The NMTO particles exhibited serious aggregation and coarsening after incubating for 60 min. In contrast, the similar structure is also observed after reacting for 15 min at 150 ºC (Fig. S5, ESI†), revealing that the reaction is an endothermal process. The FESEM and HRTEM images (Fig. S6, ESI†) exhibit that the residual product is crystalline, and the (001) plane spacing is 0.714 nm. The product is mainly composed of Na, Mn ,Ti and O, which is consistent with the NMTO phase.

In addition, the effect of the reaction time at 110 ºC on the electrical conductivity (EC) is investigated (Fig. 1i). With increasing the incubation time, the amount of NMTO is increased continuously. Comparatively, the conductivity is reduced by increasing the concentrations of NMTO. The EC of the pristine MXene powder (t=0) is ~ $0.9×10^2$ S/cm, slightly lower than the previously reported value of ~200 S/cm.[19, 20] With increasing reaction time, the EC values decrease, down to ~$2.6×10^{-2}$ S/cm when the reaction is over 15 min, and thereafter they are stable with further increasing incubation time. Therefore, considering both the amount of NMTO and the conductivity, a reaction time of 15 min is desirable at 110
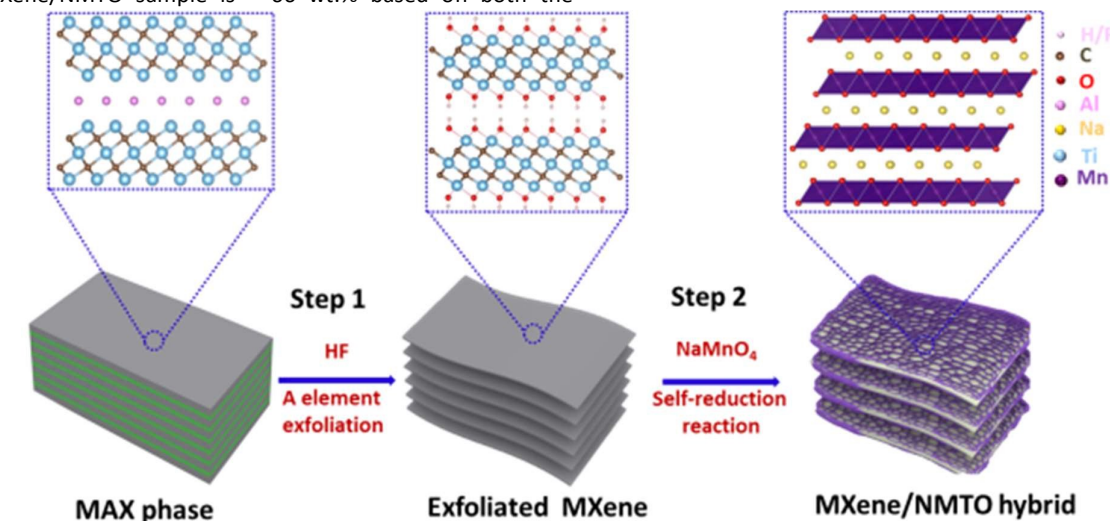
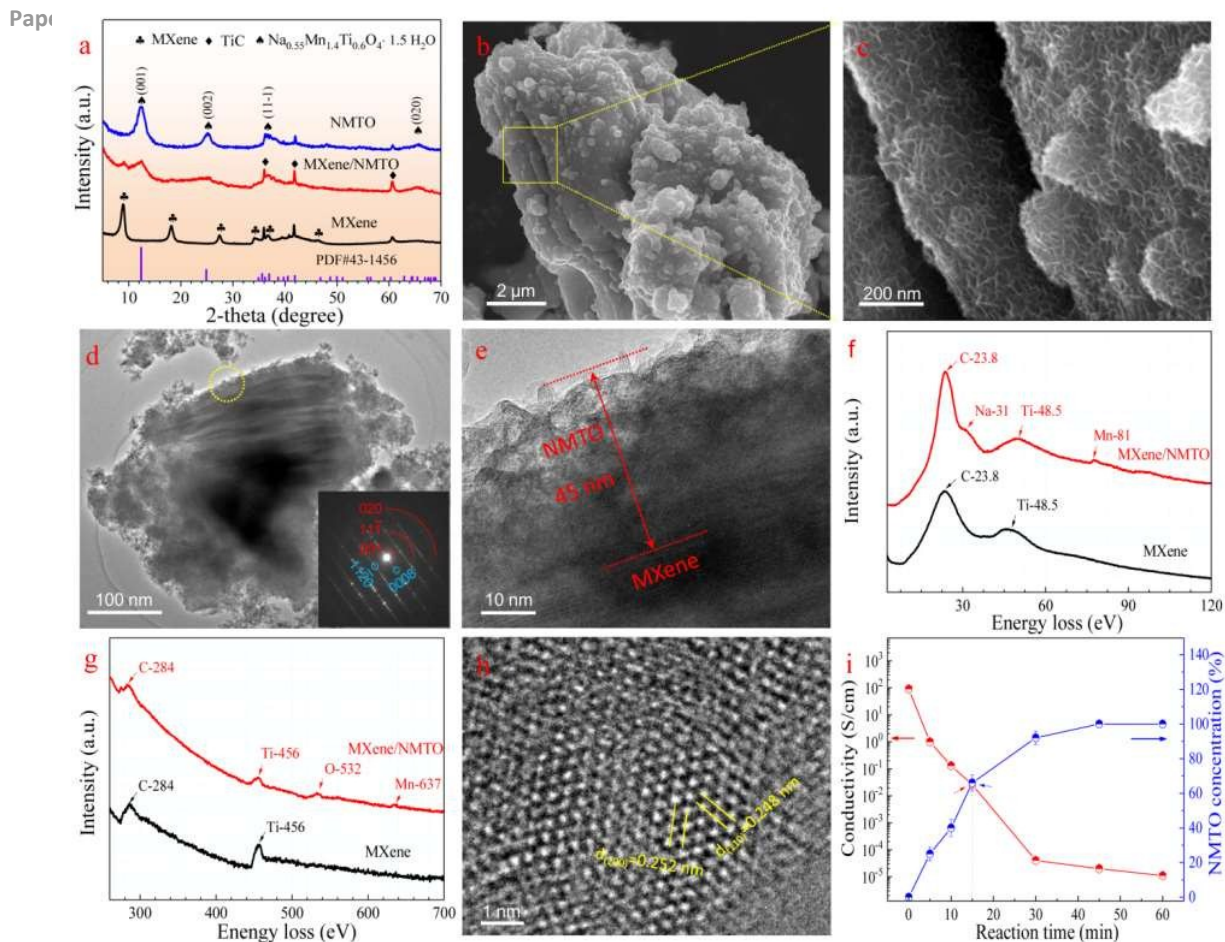**Scheme. 1** A two-step reaction process of MXene/NMTO hybrid.

Fig.1 Microstructural characterizations. (a) XRD patterns of different samples. (b) SEM image of the MXene/NMTO sample. (c) Local high magnification image of (b). (d) TEM image of the MXene/NMTO sample, the inset corresponds to its SAED pattern. (e) Local high magnification TEM image of the side area in (d). (f, g) Low-loss and core-loss EELS profiles of the MXene and the MXene/NMTO sample, respectively. (h) HRTEM image of the surface NMTO in the MXene/NMTO sample. (i) Effect of reaction time on the concentration of NMTO and the electrical conductivity of the MXene/NMTO samples.

°C, wherein an amount of 66 wt.% NMTO loading and a high EC value (2.6×10^2 S/cm) are achieved.

The self-reduction process is characterized by X-ray photoelectron spectroscopy (XPS, Fig. S7,ESI†). The distinct C1s, Ti2p and O1s spectra from the primitive MXene demonstrates the intrinsic Ti-C and Ti-O bonds,[21, 22] and the presence of Mn2p and Na1s peaks within the MXene/NMTO sample implies the loading of NMTO. As for the primitive MXene (Table S3, ESI†), the fractions of Ti(II), Ti (III) and Ti (IV) are 41.1%, 20.9% and 18.6%, respectively and the corresponding values change into 8.9%, 8.6% and 78.4% within the MXene/NMTO sample. These low valence Ti species reduce Mn^{7+} ion solution to form NMTO. The similar self-reduction role has also been confirmed in reducing Ag(I)[23, 24] or Cr(VI)[25] in alk-MXene materials. The pure NMTO spectra show that three main peaks are observed at 529.9 eV (O^{2-}) and 531.4 eV (-OH) and 533.6 eV (H_2O_{ads}) (Fig. S8 and Table S4, ESI†). Compared with the MXene/NMTO sample, the increase intensity of lattice oxygen at 529.9 eV confirms the formation of NMTO.[26] The average valence of Mn in the MXene/NMTO sample is +3.69 as obtained by fitting the XPS spectra of Mn $2p_{3/2}$ (Fig. S9 and Table S5, ESI†) using

Biesinger's reported method,[27] which is close to the theoretical value of $Na_{0.55}Mn_{1.4}Ti_{0.6}O_4$ (+3.61).

Li ion storage performance

As for Ti-doped Na-Mn-O systems, the electrochemically active Mn element serves as a redox-reaction center and provides the most of the capacity during the cycling process. However, the doping tetravalent Ti element which is confirmed by the XPS fitting results (Fig. S8 and Table S3) shows electrochemcial the electrochemical inactivity and only makes the structure of Na-Mn-O systems stable.[28] The electrochemical properties of the MXene/NMTO sample as an anode material were assessed in the half cells vs. Li+/Li. Cyclic voltammetry (CV) curves (Fig. 2a) reveal obvious reduction peaks at around 1.4 V and 0.66 V during the first cycle, which disappears in the subsequent cycles. This could be ascribed to the reduction of trace impurity possibly originated from higher oxidation state of Mn. The sharp reduction peak at 0.13-0.25 V is attributed to the reduction of Mn^{2+} to Mn. Additionally, the wide oxidation peak at 1.32-1.36 V in the anodic sweep can be assigned to the oxidation of Mn to Mn^{2+}.[12] A broad shoulder at 2.45 V shows that a higher oxidation state (>2) is obtained by oxidizing the

4 | *J. Mater. Chem. A*, 2019, **00**, 1-3

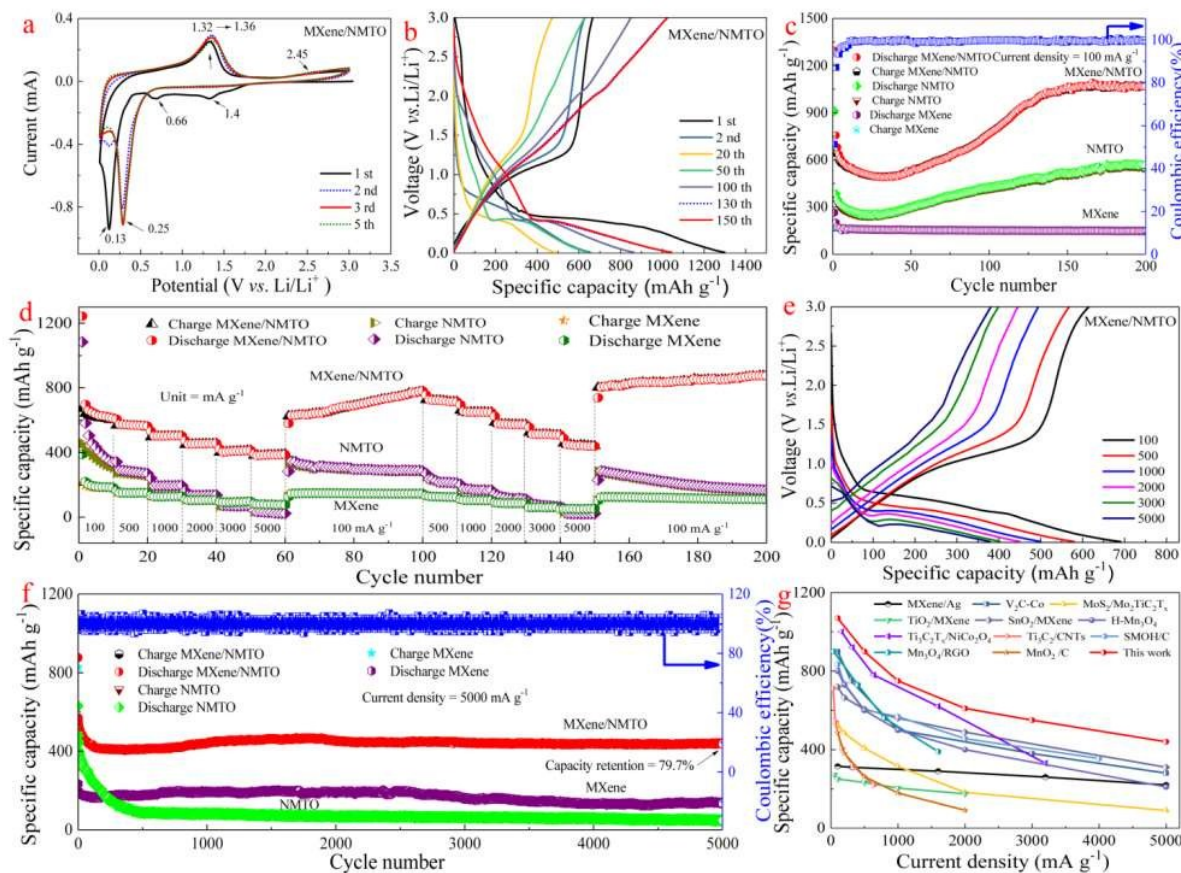This journal is © The Royal Society of Chemistry 2019

Fig. 2 Electrochemical properties of the MXene/NMTO anode. (a) CV curves of the MXene/NMTO eletrode at a scan rate of 0.2 mV s^{-1} over a voltage range of 0.01-3.0 V *vs.* Li/Li+. (b) The discharge-charge curves of the MXene/NMTO sample. (c) Cycle performances of three samples at a current density of 100 mA g^{-1}. Coulombic efficiency only involves the MXene/NMTO sample. (d) Rate properties of three samples at a current range of 100-5000 mA g-1. (e) The second discharge/charge profiles of the MXene/NMTO sample at a current density range of 100-5000 mA g^{-1}. (f) Long-term cycling performances of the MXene/NMTO electrode at a current density of 5000 mA g^{-1}. Coulombic efficiency of the MXene/NMTO electrode is spotted only. (g) Comparison of rate capacities of the MXene/NMTO composite with MXene-based and manganese oxide-based anode materials (MXene/Ag,[23] Ti$_3$C$_2$/CNTs,[30] Ti$_3$C$_2$T$_x$/NiCo$_2$O$_4$,[31] TiO$_2$/MXene,[32] SnO$_2$/MXene,[32] MoS$_2$/Mo$_2$TiC$_2$T$_x$,[33] V$_2$C-Co,[34] Mn$_3$O$_4$/RGO,[35] MnO$_2$/C,[36] SMOH/C,[37] H-Mn$_3$O$_4$[38]).

Mn^{2+}.[12, 29] The discharge/charge voltage profiles of the MXene/NMTO electrode (Fig. 2b) demonstrate that a sustained voltage plateau is observed in the discharge curves, assigned to the reduction from high valence state of Mn^{2+} to Mn, differing from bare MXene and NMTO (Fig. S10, ESI†). The cycling performance of bare MXene is rather poor, which is consistent with previous result.[23] In contrast, a notable activated process is detected in both NMTO and MXene/NMTO samples at the current density of 100 mA g^{-1} (Fig. 2c) and the activation mechanism will be discussed later. However, this activation process is eliminated for NMTO by cycling ten times at different current rates (Fig. 2d), suggesting that the high rate cycles weaken the activated process. Differing from bare MXene and NMTO, the capacity and rate performances of MXene/NMTO are further increased. With increasing current density, the capacities of three samples are slightly reduced (Fig. 2e and Fig.S11, ESI†). Note that a high capacity is achieved in the MXene/NMTO sample at a high current density, which is far higher than those of MXene and NMTO. The capacity of 440 mAh g^{-1} at a current density of 5000 mA g^{-1} can be well maintained even after 5000 cycles (79.7% capacity retention, Fig. 2f). These values overwhelm almost all other high performance MXenes-based anode

materials and most of manganese oxide-based anode materials for LIBs reported hitherto (Fig. 2g).[23, 30-38]

In addition, the electrochemical properties of the MXene/NMTO sample as a cathode material were also investigated in the half cells *vs.* Li$^+$/Li. CV curves (Fig. 3a) show a pair of redox peaks at 2.81-3.06/3.28-3.35 V which is mainly assigned to Mn^{4+}/Mn^{3+}.[39] The wide peak in the first cycle is related to the primitive Mn^{5+}/Mn^{4+} ion at 3.85/4.03 V.[39] However, the peak is eliminated in the following cycles, revealing that the main reaction of Mn^{4+}/Mn^{3+} couple accounts for cathode materials. Fig. 3b shows the typical charge/discharge cycle at the cathode side from 1.50 to 4.80 V at a current density of 100 mA g^{-1}. A reversible capacity of 170 mA h g^{-1} can be obtained in the second and following cycles, and it shows a very high average voltage, smooth charge/discharge profiles, and little polarization. The cycling stability and rate performance of MXene, NMTO and MXene/NMTO as cathode electrodes were also evaluated (Fig. 3c-e and Fig. S12-13, ESI†).

Compared with bare MXene and NMTO, the capacity, rate performance and cyclability are greatly improved in the MXene/NMTO sample. The capacity of the MXene/NMTO sample at 100 mA g^{-1} after 100 cycles is found to be 152 mAh g^{-1}, which is 3 times higher than that of the NMTO sample (54

This journal is © The Royal Society of Chemistry 2019

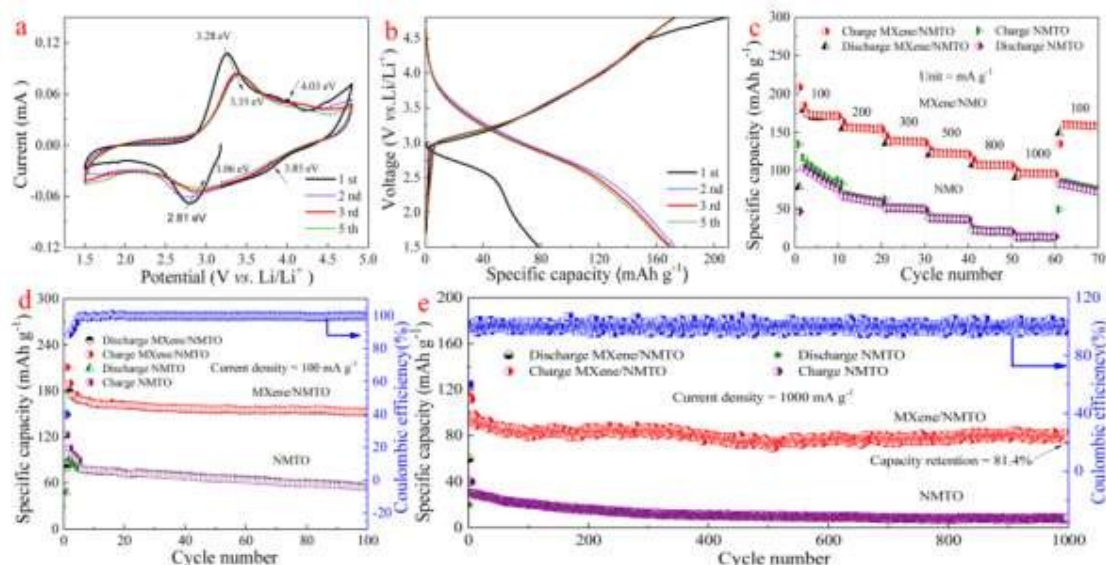*J. Mater. Chem. A*, 2019, **00**, 1-3 | **5**

Paper

Fig. 3 Electrochemical properties of the MXene/NMTO cathode. (a) CV curves of the MXene/NMTO electrode at a scan rate of 0.2 mV s^{-1} over a voltage range of 1.5-4.8 V vs Li/Li$^+$. (b) The discharge/charge curves of the MXene/NMTO sample. (c) Rate properties of three samples at a current range of 100-1000 mA g^{-1}. (d) Cycling properties of two samples at a current density of 100 mA g^{-1}. Coulombic efficiency only invloves the MXene/NMTO sample. (e) Long-term cycling performances of two samples at a current density of 1000 mA g^{-1}. Coulombic efficiency of the MXene/NMTO electrode is shown only.

mAh g^{-1}). Attractively, the capacity after 1000 cycles is very close to the initial capacity, even with the deep charging and discharging at a current density of 1000 mA g^{-1}. The corresponding capacity retention is 81.4%.

Finally, the MXene/NMTO-based full cells were assessed using a charge/discharge test (Fig. 4a). A reversible average discharge capacity of 140 mAh g^{-1} was obtained in the second and subsequent cycles (Fig. 4b) at a charge/discharge current density of 100 mA g^{-1}. More importantly, the charge/discharge

profiles are symmetrical, and no obvious polarization is observed in this well-configured symmetric full cell. The rate capability is also evaluated with different current densities of 100-1000 mA g^{-1} in Fig. 4c. The reversible capacity can be ~100 mA h g^{-1} at a current density of 500 mA g^{-1}, and it changes to ~77 mAh g^{-1} even at a current density of 1000 mA g^{-1}. As for the long cycling performance at high rate, the symmetric battery is measured at a current density of 500 mA g^{-1}, offering 79.4% of capacity retention for extensive cycling-200 times-of lithium
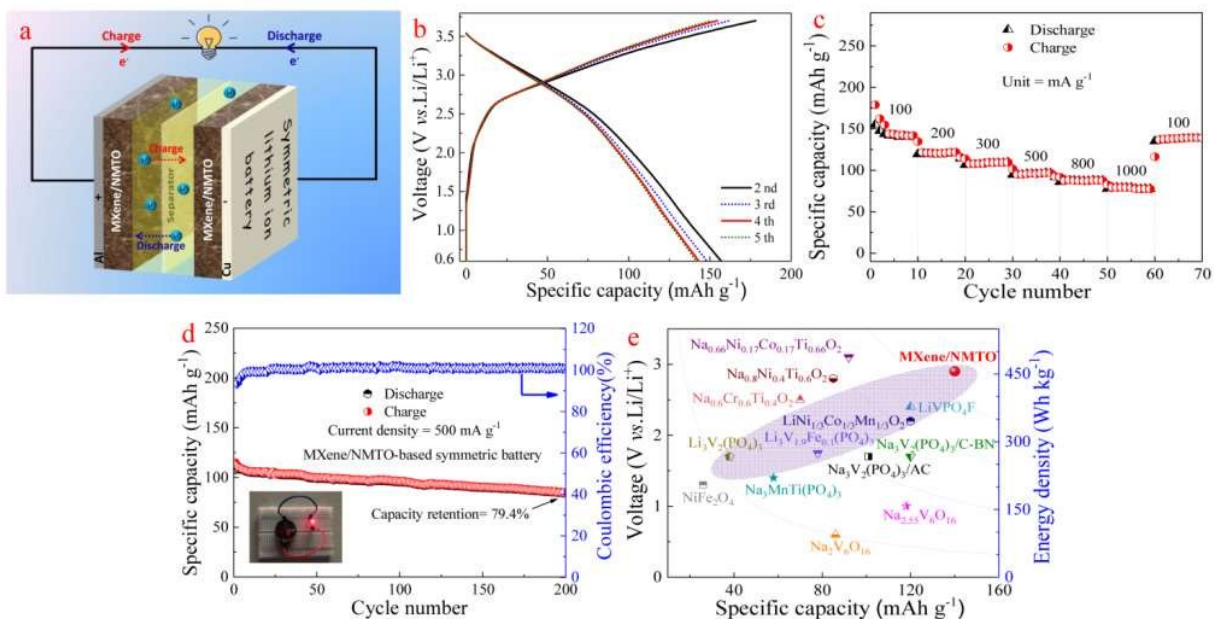

Fig. 4 Electrochemical properties of the MXene/NMTO symmetric cell. (a) Schematic diagram of the MXene/NMO||MXene/NMTO symmetric LIBs. (b) CV curves of the electrode at a scan rate of 0.2 mV s-1 over a voltage range of 0.6-3.7 V vs. Li/Li$^+$. (c) The discharge/charge curves of the full cell. (d) Rate properties and coulombic efficiency of the full cell at a current density range of 100-1000 mA g^{-1}. (e) Cycling properties of the full cell at a current density of 500 mA g-1. A capacity retention remains 79.4 % after 200 cycles. The inset shows the lighted LED bulb driven by the MXene/NMTO symmetric cell. (e) Comparison of specific capacity, average voltage, and energy density of the recently reported symmetric LIBs (mauve shadow) and SIBs (LiVPO$_4$F,[6] Li$_3$V$_2$(PO$_4$)$_3$,[7] LiNi$_{1/3}$Co$_{1/3}$Mn$_{1/3}$O$_2$,[42] Li$_3$V$_{1.9}$Fe$_{0.1}$(PO$_4$)$_3$,[43] Na$_{2.55}$V$_6$O$_{16}$,[44] Na$_{0.66}$Ni$_{0.17}$Co$_{0.17}$Ti$_{0.66}$O$_2$,[45] Na$_{0.8}$Ni$_{0.4}$Ti$_{0.6}$O$_2$,[3] Na$_{0.6}$Cr$_{0.6}$Ti$_{0.4}$O$_2$,[46] Na$_2$V$_6$O$_{16}$,[47] NiFe$_2$O$_4$,[48] Na$_3$MnTi(PO$_4$)$_3$,[49] Na$_3$V$_2$(PO$_4$)$_3$/C-BN,[50] Na$_3$V$_2$(PO$_4$)$_3$/AC[51]).

6 | *J. Mater. Chem. A*, 2019, **00**, 1-3

This journal is © The Royal Society of Chemistry 2019

extraction and insertion. The corresponding coulombic efficiency exceeds 99.1% except for the initial several cycles, and our assembled symmetric full LIBs can light a LED lamp (Fig. 4d). However, the capacity fade of the symmetric cell may be the occurrence of the manganese dissolution in the electrolyte, the decomposition of the electrolyte and Jahn-Teller distortion during the cycling,[40, 41] which can be further improved by optimizing the electrochemical performance of MXene/NMTO samples, the composition of electrolyte, the mass ratio of cathode/ anode and other critical components. As summarized in Fig. 4e, the energy density of MXene/NMTO hybrid (~393.4 Wh kg^{-1}) (the specific capacity and energy density are calculated based on the mass of cathode electrode) is the highest one among all symmetry LIBs and NIBs.[3, 6, 7, 42-51]

Reaction mechanisms

To probe the reaction kinetics, the *in-situ* TEM has been performed to study the phase evolution (Movie S1). Fig. 5a-d reveals that the diameter of NMTO expanded from 408 to 526 nm at a voltage of -6 V for 485 s when the NMTO contracted with Li metal electrode. By comparison, the particle of NMTO contracted from 526 to 475 nm at a voltage of 6 V for 539 s (Fig. 5e-h and Movie S1, ESI†). It demonstrates that Li insertion/extraction is partially reversible. The *in-situ* selected area electron diffraction (SAED) patterns (Fig. 5i-k) show that

the lattice spacings of (200), (112) and (11-4) changed slightly during the discharge/charge process, indicating that there is no additional new phase, which is consistent with the reported result.[13] The slight fluctuation of lattice spacing is attributed to the variation of fraction of different Mn valence states as revealed by EELS spectra (Fig. 5l). According to previous results,[52] the lower L_3/L_2 value corresponds to a higher faction of high-valence Mn. The shift toward low energy (2.8 eV) for the Mn-L_3 edge and a higher L_3/L_2 value indicate the increased amount of low- valence Mn during the discharge process.[53]

The reversion in both the edge energy and peak of the EELS spectra verified the increment of high-valence Mn during the charge process. This process was also confirmed by XPS. Fig. 6a shows the characteristic peaks of Mn2p after 100 cycles as anode shift 1.2 eV toward high energy direction, indicating that a high oxidation state of Mn is obtained. The trend is also supported by the increased concentration of lattice oxygen (67.8%, Fig. 6b).[13] In contrast, the fraction of high valence Mn is remarkably reduced, but the values of low valence Mn is increased which corresponds to the cathode electrode after 100 cycles. This process can also be confirmed by the reduced lattice oxygen (20.2%, Fig. 6b).[54]

Compared with the other two samples, an activation process for the anode MXene/NMTO electrode during the cycle process is detected. The main reasons are associated with
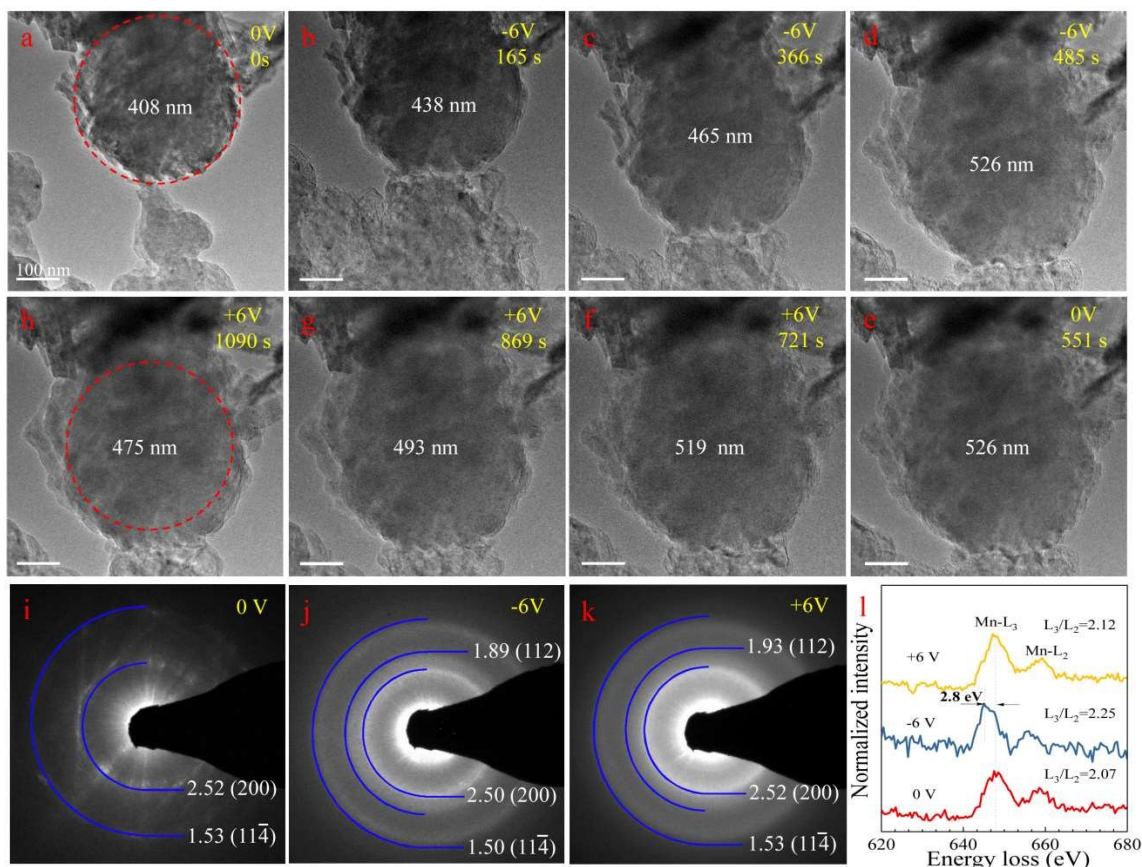

Fig. 5 In-situ microstructural features during the discharge/charge processes. (a-d) Typical morphology variation of the NMTO electrodes during discharge process. (e-h) Typical morphology change of the NMTO electrode during charge process. *In-situ* SAED patterns of the primitive (i), discharged (j) and charged (k) NMTO electrodes. (l) The EELS spectra of NMTO.
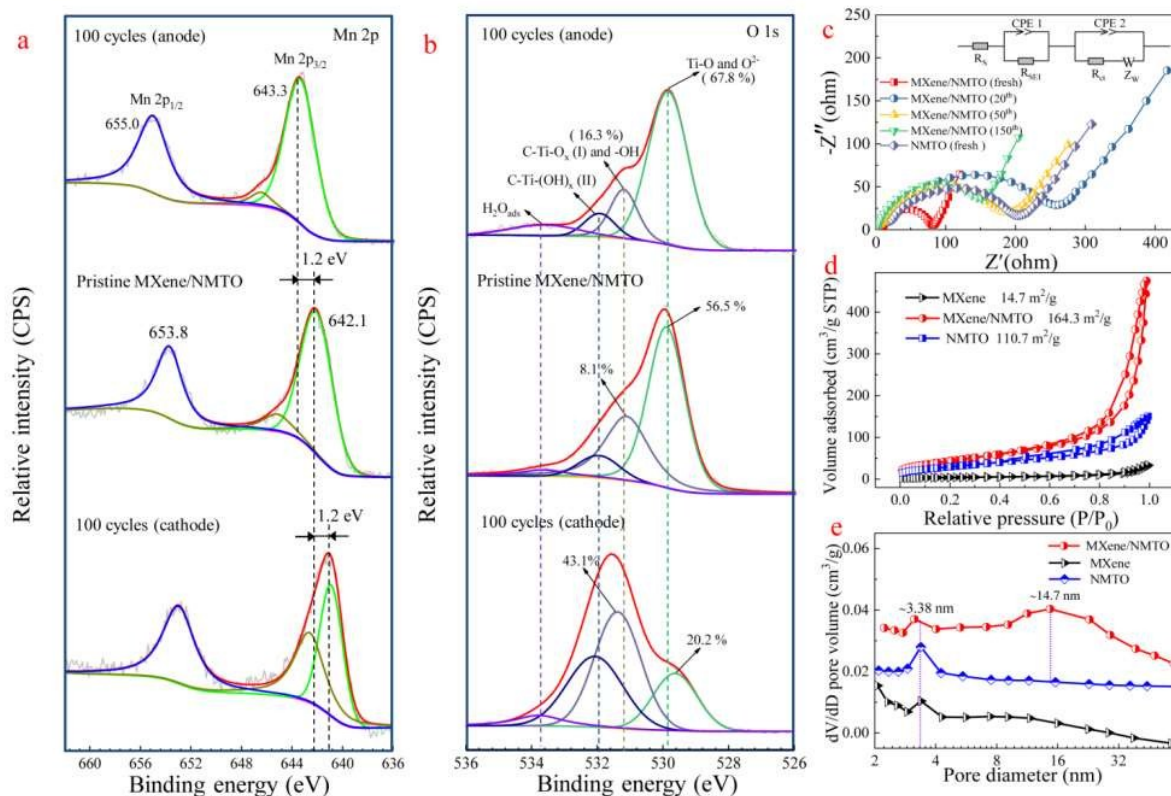
Fig. 6 Reaction mechanisms. XPS profiles of the samples after 100 cycles, (a) Mn 2p spectra, (b) O 1 spectra. Compared with the pristine MXene/NMTO sample. The cathode spectra after cycling shift toward low energy direction, but the anode spectra shift toward high energy direction. (c) EIS of different samples after different cycles. The inset corresponds to the fitting circuit. (d) Nitrogen adsorption-desorption isotherms and (e) the pore size distribution of three samples.

two aspects. On one hand, with increasing the cycle number, the volcano-shape trend of charge-transfer resistance (R_{ct}) is detected in the MXene/NMTO sample (Fig. 6c, Table S6, ESI†), suggesting the conductivity is increased during the cycling process. On the other hand, the SEM images (Fig. S14, ESI†) show the surface of well-distributed morphologies of NMTO particles even after hundreds cycles.[23, 55] The HRTEM images (Fig. S15, ESI†) show that the dimension of NMTO particles is reduced, and some fine particles are homogeneous on the surface. Owing to the existence of the MXene substrate, the fine particles can be effectively dispersed, thus the number of effective sites in NMTO layer increases with increasing the surface area. As a result, the capacity is greatly improved. Simultaneously, the (001) lattice spacing remains intact during the cycling process, accounting for good rate performance by facilitating ion diffusion.

In addition, the high capacity and good rate performances of the MXene/NMTO hybrid are also related to the specific surface area and pore-size distribution of the heterogeneous materials. Firstly, compared with pristine MXene (14.7 m² g⁻¹) and NMTO (110.7 m² g⁻¹), forming the MXene/NMTO hybrid sample has the largest BET surface areas of ~164.3 m² g⁻¹ (Fig. 6d), offering more adsorbed sites for Li storage. Secondly, differing from bare MXene and NMTO samples, both fine pores (~3.38 nm) and coarse pores (~14.7 nm) (Fig. 6e) are detected in the MXene/NMTO sample. The hierarchical structure in pore distribution, especial wide pore dimension, accelerates ion transformation, improving both capacity and

rate performance. Therefore, the high capacity, rate performance and kinetics of the dipolar MXene/NMTO electrodes in a wide current range are mainly related to high conductivity, multiple valence Mn and large bimodal meso-pore structure.

Conclusions

In summary, a new MXene/NMTO hybrid has been synthesized by a simple microwave-assisted reaction based on the self-reduction role of MXene. The crystal structure and reaction process were clarified by environmental spherical aberration-corrected electron microscopy. The redox couples of Mn^{2+}/Mn and Mn^{4+}/Mn^{3+} account for anode and cathode reactions, respectively. Using this low-cost bipolar electrode, a lithium ion full cell was tailored to meet the demand of energy storage. This full cell shows the highest energy density of 393.4 Wh kg⁻¹ of all symmetric LIBs and NIBs, and the highest average voltage of 2.81 V in all the studies on symmetric LIBs full cells. These results on a low cost, high efficiency, high energy density and high voltage lithium ion full cell will greatly contribute to the energy storage technology, and will also provide new avenues for designing advanced LIBs.

Conflicts of interest

There are no conflicts to declare.

8 | *J. Mater. Chem. A*, 2019, **00**, 1-3

This journal is © The Royal Society of Chemistry 2019

View Article Online
DOI: 10.1039/C9TA00744J

Acknowledgements

References

1   N. Nitta, F. Wu, J. T. Lee and G. Yushin, *Mater. Today*, 2015, **18**, 252.
2   V. Palomares, P. Serras, I. Villaluenga, K. B. Hueso, J. Carretero-González and T. Rojo, *Energy Environ. Sci*., 2012, **5**, 5884.
3   S. Guo, H. Yu, P. Liu, Y. Ren, T. Zhang, M. Chen, M. Ishida and H. Zhou, *Energy Environ. Sci*., 2015, **8**, 1237.
4   Y. Zhang, H. Zhao and Y. Du, *J. Mater. Chem. A*, 2016, **4**, 7155.
5   C. H. Chen, J. Liu and K. Amine, *J. Power Sources*, 2001, **96**, 321-328.
6   J. Barker, R. K. B. Gover, P. Burns and A. Bryan, *Solid-State Lett.*, 2005, **8**, A285.
7   E. Kobayashi, L. S. Plashnitsa, T. Doi, S. Okada and J.-i. Yamaki, *Electrochem. Commun.*, 2010, **12**, 894.
8   J. C. Burns, L. J. Krause, D.B. Le, L. D. Jensen, A. J. Smith, D. Xiong and J. R. Dahn, *J. Electrochem. Soc.*, 2011, **158**, A1417.
9   V. Nair, Y. Cheah and Madhavi, S., *J. Electrochem. Soc.*, 2013, **161**, A256.
10 L. Zhang, S. X. Dou, H. K. Liu, Y. Huang and X. Hu, *Adv. Sci.*, 2016, **3**, 1600115.
11 M. Nakayama, T. Kanaya, J.-W. Lee and B. N. Popov, *J. Power Sources*, 2008, **179**, 361.
12 J. Zhang, T. He, W. Zhang, J. Sheng, I. S. Amiinu, Z. Kou, J. Yang, L. Mai and S. Mu, *Adv. Energy Mater.*, 2017, **7**, 1602092.
13 A. K. Thapa, B. Pandit, R. Thapa, T. Luitel, H. S. Paudel, G. Sumanasekera, M. K. Sunkara, N. Gunawardhana, T. Ishihara and M. Yoshio, *Electrochim. Acta,* 2014, **116**, 188.
14 G. Zou, B. Liu, J. Guo, Q. Zhang, C. Fernandez and Q. Peng, *ACS Appl. Mater. Interfaces*, 2017, **9**, 7611.
15 Q. Peng, J. Guo, Q. Zhang, J. Xiang, B. Liu, A. Zhou, R. Liu and Y. Tian, *J. Am. Chem. Soc.*, 2014, **136**, 4113.
16 Q. Jin, N. Zhang, C. Zhu, H. Gao and X. Zhang, *Nanoscale*, 2018, **10**, 16935.
17 G. Zou, J. Guo, Q. Peng, A. Zhou, Q. Zhang and B. Liu, *J. Mater. Chem. A*, 2016, **4**, 489.
18 X. Shan, N. Zhang, R. Zheng, H. Gao and X. Zhang, *Electrochim. Acta*, 2019, **295**, 286.
19 M. Ghidiu, M. R. Lukatskaya, M. Zhao, Y. Gogotsi and M. W. Barsoum, *Nature*, 2014, **516**, 78.
20 F. M. Römer, U. Wiedwald, T. Strusch, J. Halim, E. Mayerberger, M. W. Barsoum and M. Farle, *RSC Adv.*, 2017, **7**, 13097.
21 Q. Fua, J. Wen, N. Zhang, L. Wu, M. Zhang, S. Lin, H. Gao and X. Zhang, *RSC Adv.*, 2017, **7**, 11998.
22 L. Li, M. Zhang, X. Zhang and Z. Zhang, *J. Power Sources*, 2017, **364**, 234.
23 G. Zou, Z. Zhang, J. Guo, Liu, B. Q. Zhang, C. Fernandez and Q. Peng, *ACS Appl. Mater. Interfaces*, 2016, **8**, 22280.
24 Z. Zhang, H. Li, G. Zou, C. Fernandez, B. Liu, Q. Zhang, J. Hu and Q. Peng, *ACS Sustain. Chem. Eng.*, 2016, **4**, 6763.
25 Y. Ying, Y. Liu, X. Wang, Y. Mao, W. Cao, P. Hu and X. Peng, *ACS Appl. Mater. Interfaces*, 2015, **7**, 1795.
26 D. Banerjee and H. W. Nesbitt, *Geochim. Cosmochim. Acta*, 1999, **63**, 3025.
27 M. C. Biesinger, B. P. Payne, A. P. Grosvenor, L. W. M. Lau, A. R. Gerson and R. S. C. Smart, *Appl. Surf. Sci.*, 2011, **257**, 2717.
28 F. Zhang, W. Li, X. Xiang, M. Sun, *J. Electroanal. Chem.*, 2017, **802**, 22.
29 J. Li, J. Yu, I. S. Amiinu, J. Zhang, J. Sheng, Z. Kou, Z. Wang, Q. Yu, L. Mai and S. Mu, *J. Mater. Chem. A*, 2017, **5**, 18509.
30 Y. Liu, W. Wang, Y. Ying, Y. Wang and X. Peng, *Dalton Trans.*, 2015, **44**, 7123.
31 M. Zhao, M. Torelli, C. Ren, M. Ghidiu, Z. Ling, B. Anasori, M. W. Barsoum and Y. Gogotsi, *Nano Energy*, 2016, **30**, 603.
32 Y. Liu, P. Zhang, N. Sun, B. Anasori, Q. Zhu, H. Liu, Y. Gogotsi and B. Xu, *Adv. Mater*., 2018, **30**, 1707334.
33 C. Chen, X. Xie, B. Anasori, A. Sarycheva, T. Makaryan, M. Zhao, P. Urbankowski, L. Miao, J. Jiang and Y. Gogotsi, *Angew. Chem. Int. Ed*., 2018, **57**, 1846.
34 C. Wang, H. Xie, S. Chen, B. Ge, D. Liu, C. Wu, W. Xu, W. Chu, G. Babu, P. M. Ajayan and L. Song, *Adv. Mater*., 2018, **30**, 1802525.
35 H. Wang, L. Cui, Y. Yang, H. S. Casalongue, J. T. Robinson, Y. Liang, Y. Cui and H. Dai, *J. Am. Chem. Soc.*, 2010, **132**, 13978.
36 Z. Cai, L. Xu, M. Yan, C. Han, L. He, K. M. Hercule, C. Niu, Z. Yuan, W. Xu, L. Qu, K. Zhao and L. Mai, *Nano Lett*., 2015, **15**, 738.
37 J. Li, J. Yu, I. S. Amiinu, J. Zhang, J. Sheng, Z. Kou, Z. Wang, Q. Yu, L. Mai and S. Mu, *J. Mater. Chem. A*, 2017, **5**, 18509.
38 X. Liu, J. Piao, D. Bin, T. Zhang, S. Duan, Z. Wu, A. Cao and L. Wan, *Chem. Commun*., 2017, **53**, 2846.
39 M. Freire, N. V. Kosova, C. Jordy, D. Chateigner, O. I. Lebedev, A. Maignan and V. Pralong, *Nat. Mater*., 2016, **15**, 173.
40 J. Lu, C. Zhan, T. Wu, J. Wen, Y. Lei, A. J. Kropf, H. Wu, D. J. Miller, J. W. Elam, Y. K. Sun, X. Qiu and K. Amine, *Nat. Commun*., 2014, **5**, 5693.
41 X. Li, X. Ma, D. Su, L. Liu, R. Chisnell, S. P. Ong, H. Chen, A. Toumar, J. C.Idrobo, Y. Lei, J. Bai, F. Wang, J. W. Lynn, Y.S. Lee and G. Ceder, *Nat. Mater*., 2014, **13**, 586.
42 J. J. Woo, V. A. Maroni, G. Liu, J. T. Vaughey, D. J. Gosztola, K. Amine and Z. Zhang, *J. Electrochem. Soc.*, 2014, **161**, A827.
43 P. Ping, Q. S. Wang, J. H. Sun, X. Xia, J. R. Dahn, *J. Electrochem. Soc*., 2012, **159**, A1467.
44 S. Hartung, N. Bucher, V. S. Nair, C. Y. Ling, Y. Wang, H. E. Hoster and M. Srinivasan, *Chem. Phys. Chem*., 2014, **15**, 2121.
45 S. Guo, P. Liu, Y. Sun, K. Zhu, J. Yi, M. Chen, M. Ishida and H. Zhou, *Angew. Chem. Int. Ed*., 2015, **54**, 11701.
46 Y. Wang, R. Xiao, Y.-S. Hu, M. Avdeev and L. Chen, *Nat. Commun*., 2015, **6**, 6954.
47 S. Yuan, Y. Zhao and Q. Wang, *J. Alloys Compd.*, 2016, **688**, 55.
48 J. Shao, X. Li, Y. Ding, Z. Wan, H. Liu, J. Yun, Y. Liu, Q. Qu and H. Zheng, *Electrochem. Commun.*, 2014, **40**, 9.
49 H. Gao and J. B. Goodenough, *Angew. Chem. Int. Ed.*, 2016, **55**, 12768.
50 Y. Jiang, X. Zhou, D. Li, X. Cheng, F. Liu and Y. Yu, *Adv. Energy Mater*., 2018, **8**, 1800068.
51 S. Li, Y. Dong, L. Xu, X. Xu, L. He and L. Mai, *Adv. Mater*., 2014, **26**, 3358.
52 Z. L. Wang, J. S. Yin and Y. D. Jiang, Micron, 2000, **31**, 571-580.
53 D. Tang, Y. Sun, Z. Yang, L. Ben, L. Gu and X. Huang, *Chem. Mater*., 2014, **26**, 3535.
54 C. Zhang, C. Feng, Zhang, P. Z. Guo, Z. Chen, S. Li and H. Liu, *RSC Adv.*, 2012, **2**, 1643.
55 Y. Xu, J. Guo and C. Wang, *J. Mater. Chem.*, 2012, **22**, 9562.

Journal of Materials Chemistry A

PAPER

Self-reductive synthesis of MXene/Na$_{0.55}$Mn$_{1.4}$Ti$_{0.6}$O$_4$ hybrids for high-performance symmetric lithium ion batteries
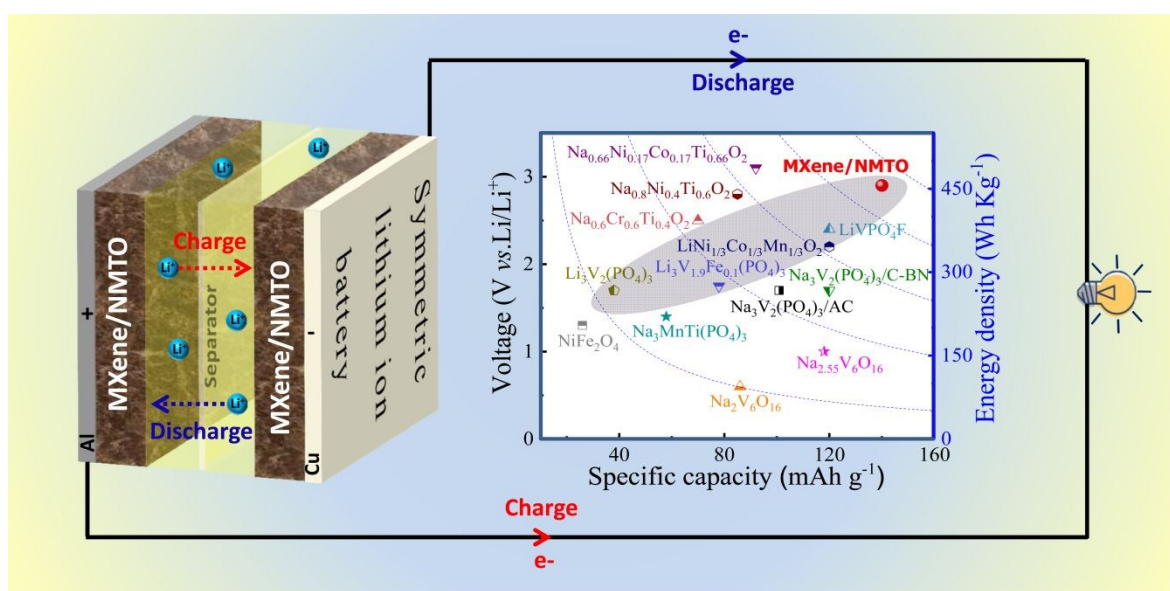
Guodong Zou[a], Bingcheng Ge[a], Hao Zhang[a], Qingrui Zhang[b], Carlos Fernandez[c], Wen Li[d], Jianyu Huang[a] and Qiuming Peng*[a]

Table of Contents

A new MXene/Na$_{0.55}$Mn$_{1.4}$Ti$_{0.6}$O$_4$ hybrid with bifunctional properties is synthesized by a self-reduction method, providing a high energy density for symmetric LIBs.

a. State Key Laboratory of Metastable Materials Science and Technology, Yanshan University, Qinhuangdao 066004, China. E-mail: pengqiuming@ysu.edu.cn
b. Hebei Key Laboratory of Applied Chemistry, School of Environmental and Chemical Engineering, Yanshan University, Qinhuangdao 066004, China.
c. School of Pharmacy and Life Sciences, Robert Gordon University, Aberdeen, AB107GJ, UK.
d. Institute of Energy Resources, Hebei Academy of Sciences, Shijiazhuang, 050081, China.
† Electronic Supplementary Information (ESI) available: Additional details and supplementary results. See DOI: 10.1039/x0xx00000x

Journal of Materials Chemistry A Accepted Manuscript

This journal is © The Royal Society of Chemistry 2019

J. Mater. Chem. A, 2019, 00, 1-3 | 1

Table S1. Chemical compositions of three samples based on ICP analysis.

Samples	Elemental composition (mg/L)			$Na_{0.55}Mn_{1.4}Ti_{0.6}O_4 \cdot 1.5\ H_2O$ (wt.%)
	Ti	Mn	Na	
MXene	70.641	-	-	0
MXene/NMTO	33.564	24.541	4.037	66.06
NMTO	15.263	36.516	6.121	~98.15
NMTO(s)	-	0.968	2.834	0

Notes: NMTO(s) is the reaction solution for the NMTO sample at 150°C for 15 min.

Table S2. Chemical compositions of three samples in terms of EDX analysis.

Samples	Elemental percentage (wt.%)						$Na_{0.55}Mn_{1.4}Ti_{0.6}O_4 \cdot 1.5 H_2O$ (wt.%)
	Ti	Mn	Na	O	C	F	
MXene	70.92	-	-	6.16	11.95	10.97	0
MXene/NMTO	33.48	24.59	4.04	30.12	4.19	3.58	~66.17
NMTO	15.25	36.48	6.01	41.81	0.45	-	~98.05

Table S3. XPS peak fitting results for Ti $2p_{3/2}$ ($2p_{1/2}$) in MXene, MXene/NMTO and NMTO samples.

Samples	BE (eV)	Fraction (%)	Assigned to
MXene	454.0	19.4	Ti-C
	455.8 (461.3)	41.1	Ti (II)
	457.2 (463.0)	20.9	Ti (III)
	459.2 (464.8)	18.6	Ti (IV)
MXene/NMTO	454.3	4.1	Ti-C
	455.8 (461.1)	8.9	Ti (II)
	457.2 (463.0)	8.6	Ti (III)
	459.2 (464.9)	78.4	Ti (IV)
NMTO	459.1 (464.8)	100	Ti (IV)

Table S4. XPS peak fitting results for O 1s in MXene, MXene/NMTO and NMTO samples.

Samples	BE (eV)	Fraction (%)	Assigned to
MXene	530.1	16.2	Ti-O
	531.2	50.5	C-Ti-O$_x$
	532.1	30.2	C-Ti-(OH)$_x$
	533.7	3.1	H$_2$O$_{ads}$
MXene/NMTO	529.9	56.5	Ti-O and O^{2-}
	531.2	31.5	-OH and C-Ti-O$_x$
	532.0	8.1	C-Ti-(OH)$_x$
	533.7	3.9	H$_2$O$_{ads}$
NMTO	529.9	66.2	O^{2-}
	531.4	25.7	-OH
	533.6	8.1	H$_2$O$_{ads}$

Table S5. Mn (2p$_{3/2}$) peak parameters for Mn in the pristine MXene/NMTO

Samples	BE (eV)	FWHW (eV)	Fraction (%)
Mn^{2+}	640.2	1.21	4.75
	641.1	1.21	0.80
	642.1	1.21	0.80
	643.0	1.21	0.75
	644.2	1.21	0.06
Mn^{3+}	641.2	1.25	15.16
	641.6	1.25	0.71
	642.7	1.25	0.74
	644.7	1.25	0.09
	645.1	1.25	0.07
Mn^{4+}	642.3	1.25	34.04
	643.2	1.3	20.50
	644.1	1.3	12.39
	645.3	1.3	6.52
	646.4	1.25	2.62

Table S6. The fitting data on the EIS curves.

Samples	R_s	R_{ct}
MXene/NMTO (fresh)	7.781	73.73
NMTO (fresh)	12.83	193.9
MXene/NMTO (20th)	12.98	210.7
MXene/NMTO (50th)	11.12	198.6
MXene/NMTO (150th)	8.475	163.7
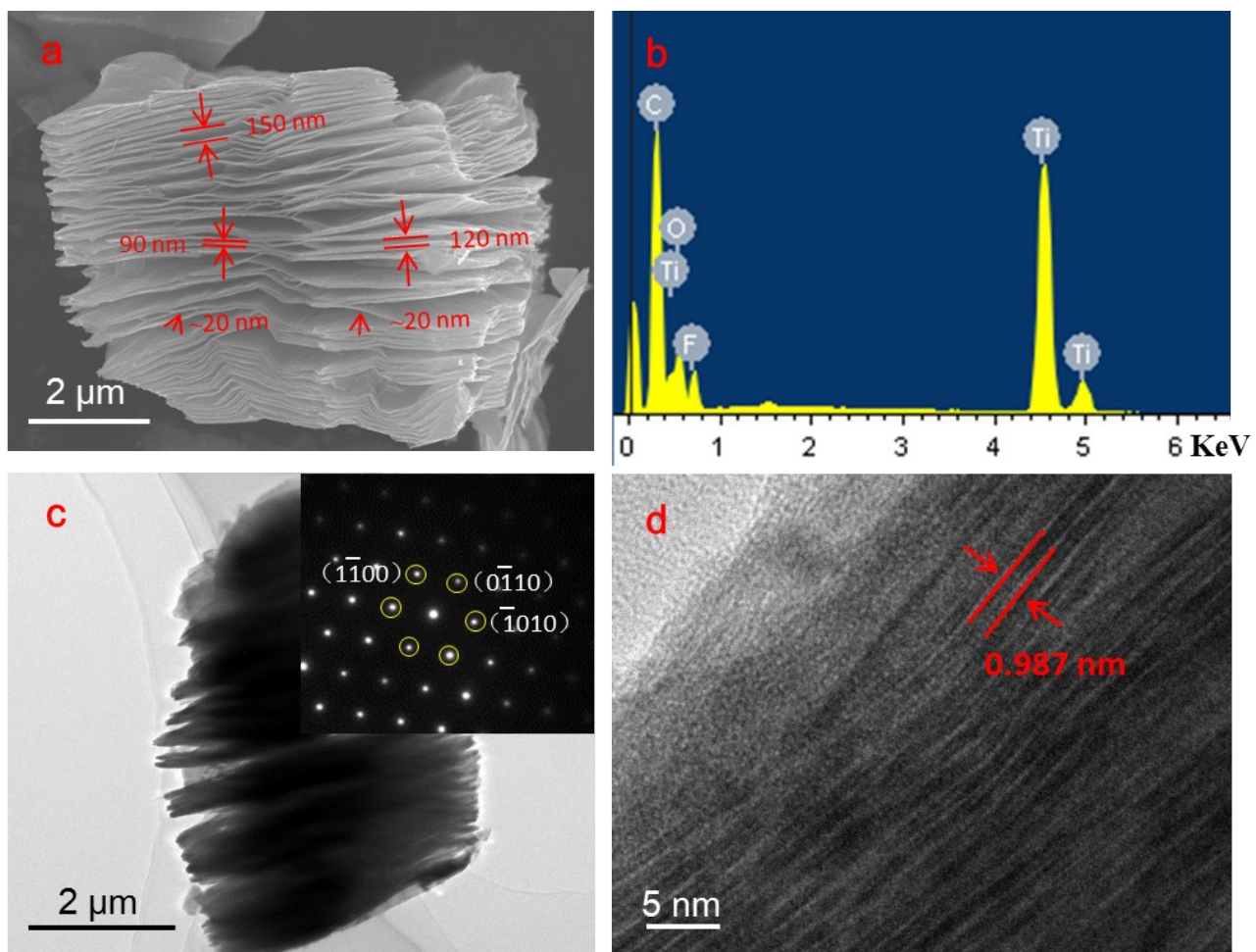
Fig. S1 (a) SEM image of MXene. (b) Elemental composition of MXene. (c) TEM image and

SAED patterns of MXene. (d) Typical HRTEM image of MXene.
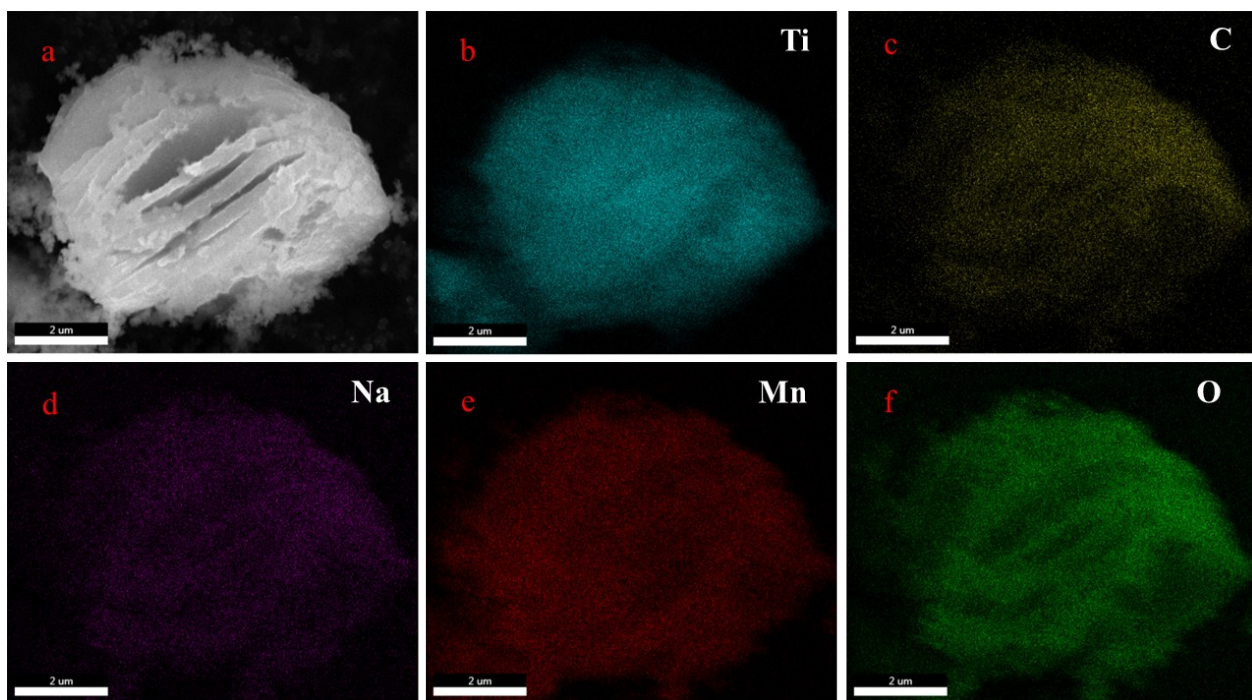
Fig. S2 (a) SEM image of the MXene/NMTO sample. (b)-(f) Elemental distribution of the

MXene/NMTO sample.
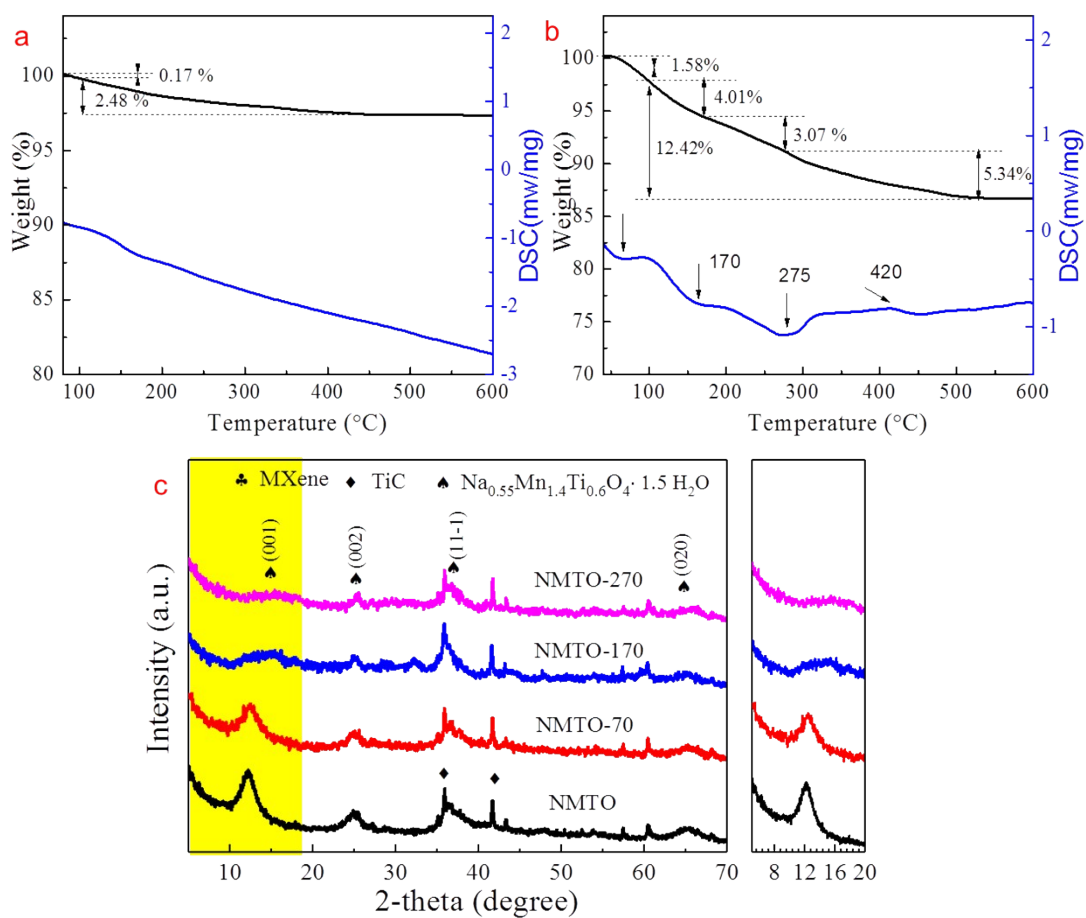
Fig. S3 Thermogravimetric analysis of MXene (a) and MXene/NMTO (b). (c) XRD patterns of

NMTO samples after annealed at different temperatures.
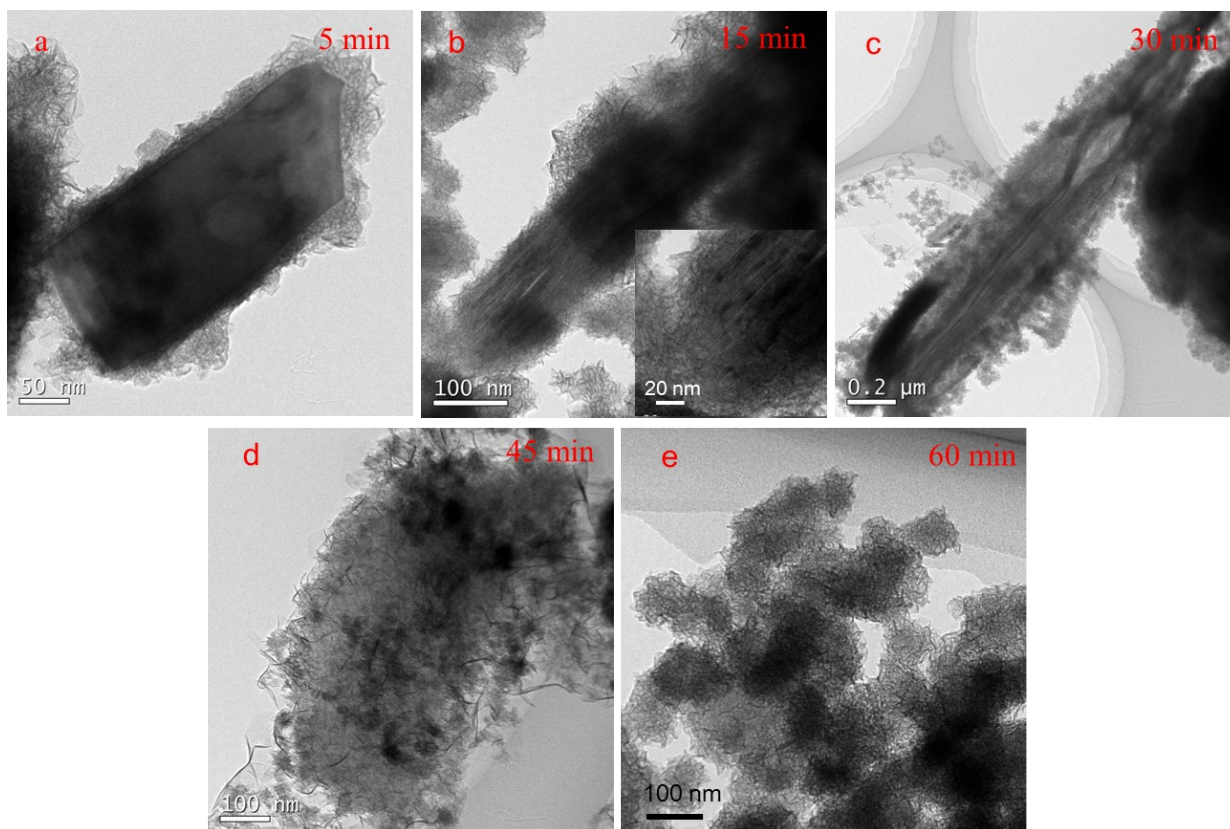
Fig. S4 The morphology evolution processes of MXene in NaMnO$_4$ solution at 110 ^{o}C for different incubation intervals.
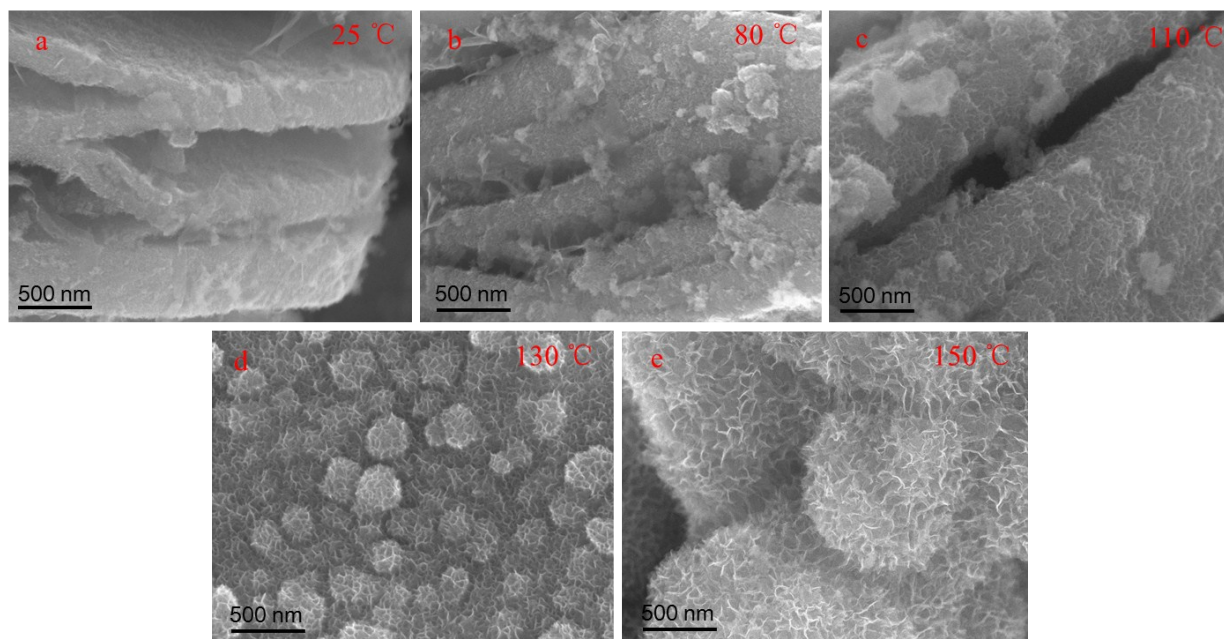
Fig. S5 The morphology evolution processes of MXene in NaMnO$_4$ solution at different reaction temperatures for 15 min.
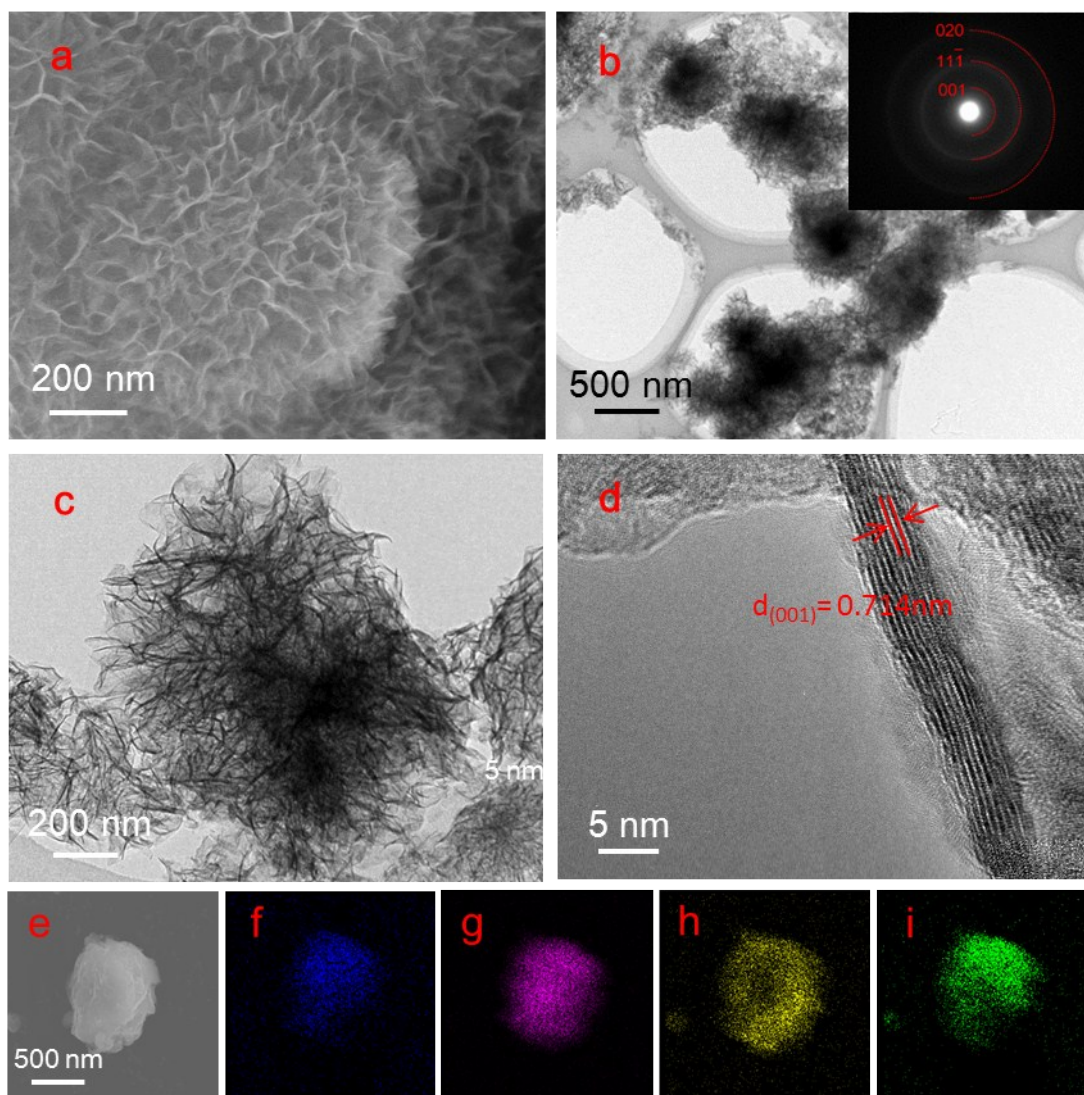
Fig. S6 Nanoflower morphology of the NMTO. (a) FESEM image, (b) TEM image and SAED (b inset), (c) and (d) HRTEM images of the NMTO sample. FESEM image (e) and corresponding EDS mapping images of Na (f), Mn (g), Ti (h) and O (i).
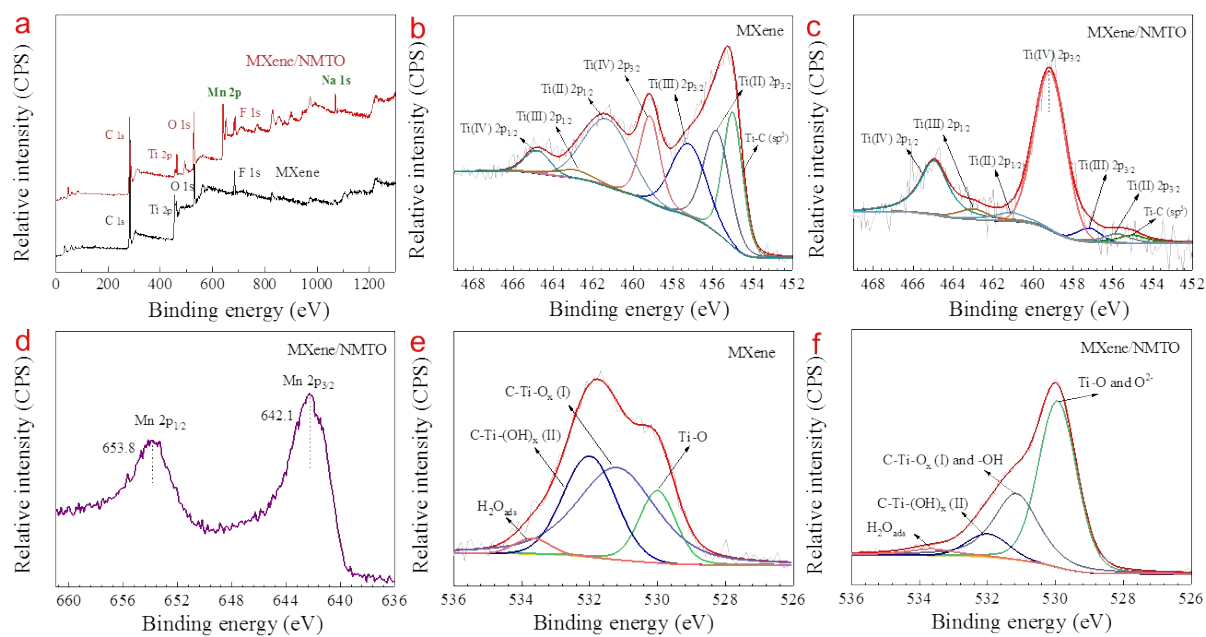
Fig. S7 XPS spectra for the MXene/NMTO hybrid. (a) The XPS survey spectrum of the samples.

Ti 2*p* spectra of the pristine MXene (b) and the MXene/NMTO hybrid (c), respectively. (d) Mn 2*p*

spectra of the MXene/NMTO hybrid. O 1*s* spectra of the pristine MXene (e) and MXene/NMTO

hybrid (f), respectively.
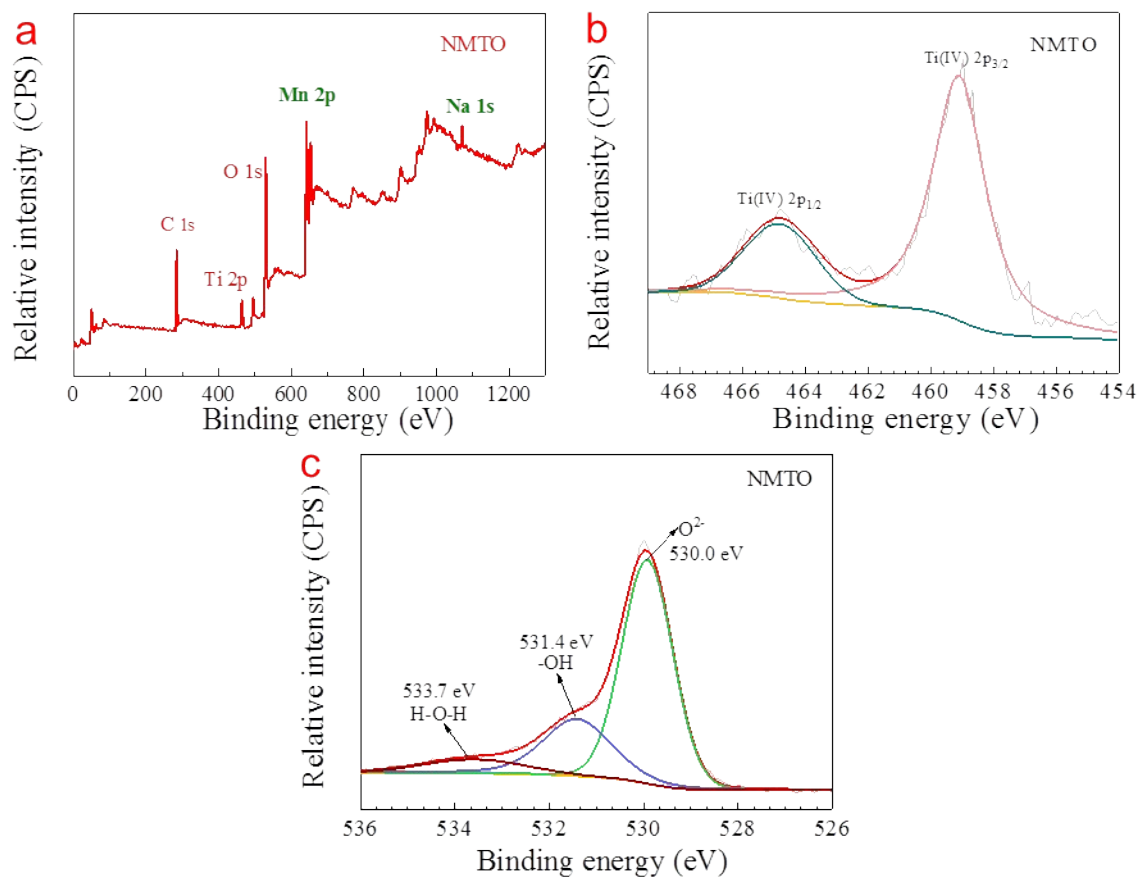
Fig. S8 (a) XPS spectra of NMTO (15 min, 150 °C). (b) Ti 2*p*, (c) O1*s* spectra of the NMTO sample.
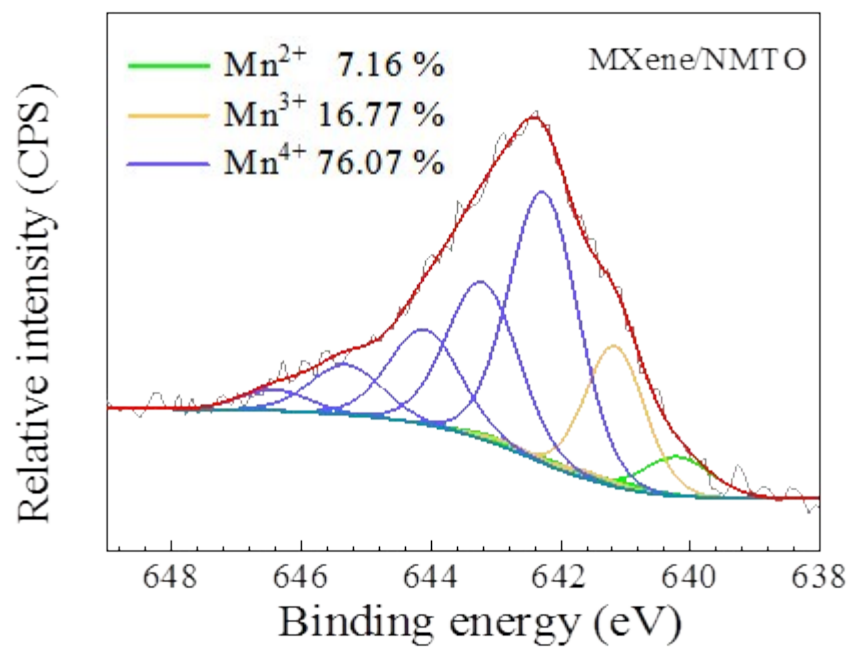
Fig. S9 Mn 2p$_{3/2}$ spectra and its fitting results of the MXene/NMTO sample.
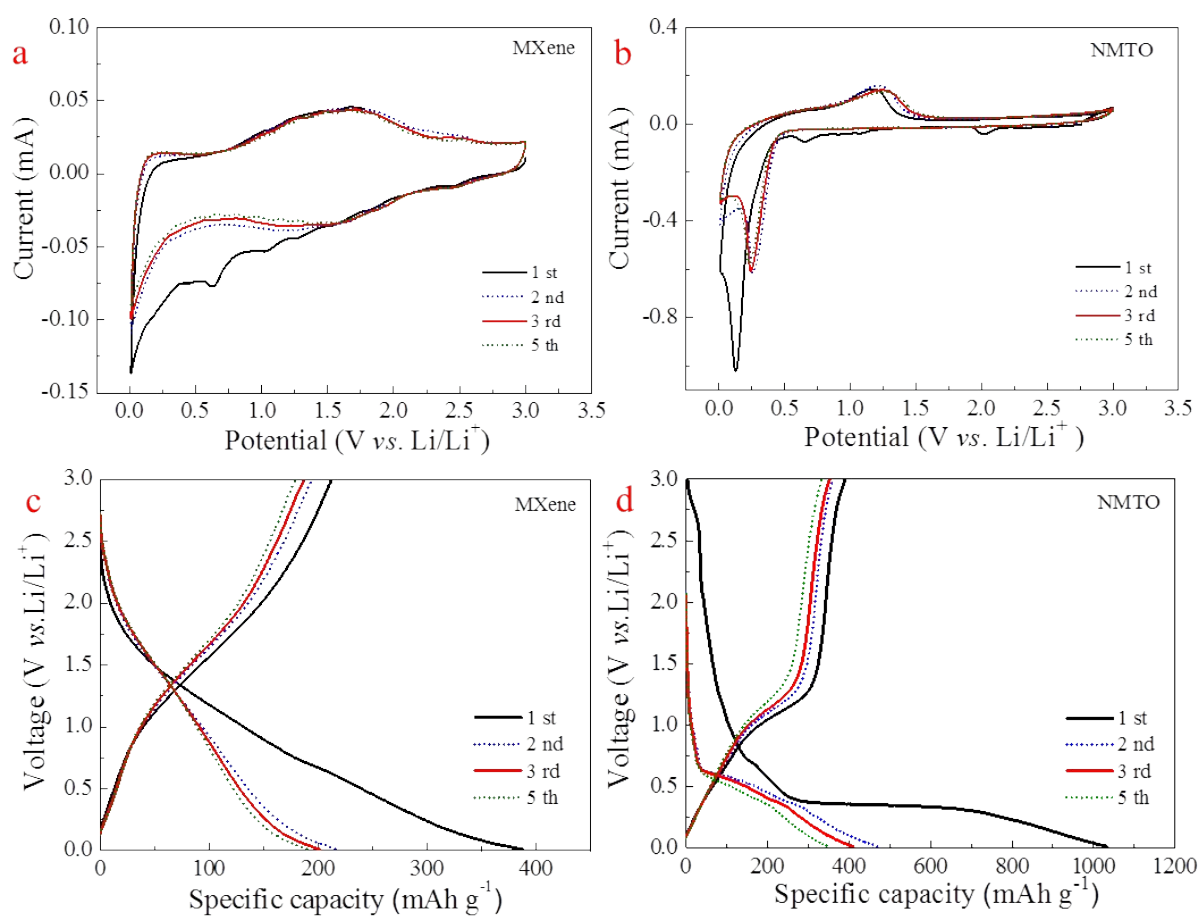
Fig. S10 CV curves of anodes at a scan rate of 0.2 mV s^{-1} over a voltage range of 0.01-3.0 V *vs* Li/Li$^+$, (a) MXene and (b) NMTO. Charge-discharge profiles of anodes at current density of 100 mA g^{-1}, (c) MXene and (d) NMTO.
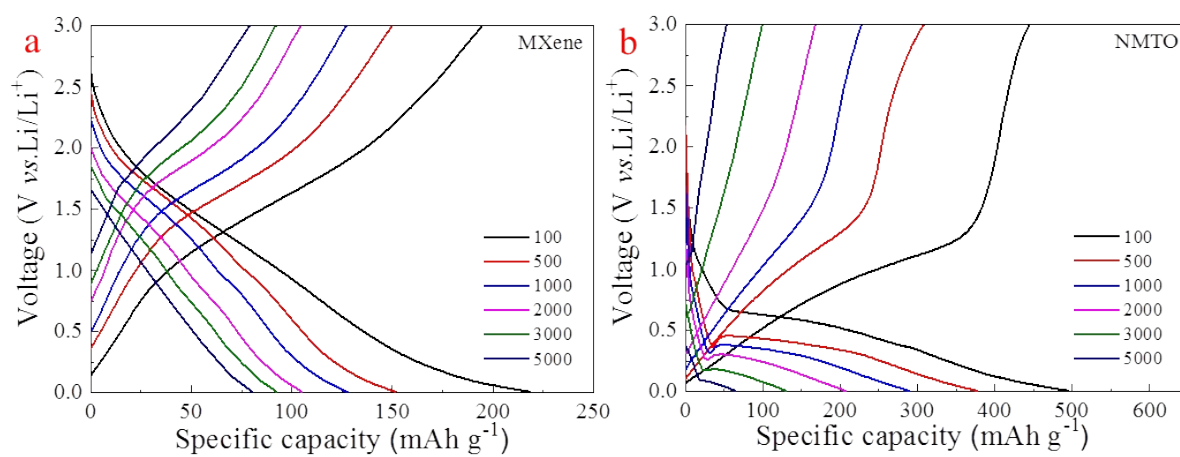
Fig. S11 The second charge-discharge profiles of MXene (a) and NMTO (b) at current density of 100-5000 mA g^{-1} over a voltage range of 0.01-3.0 V.
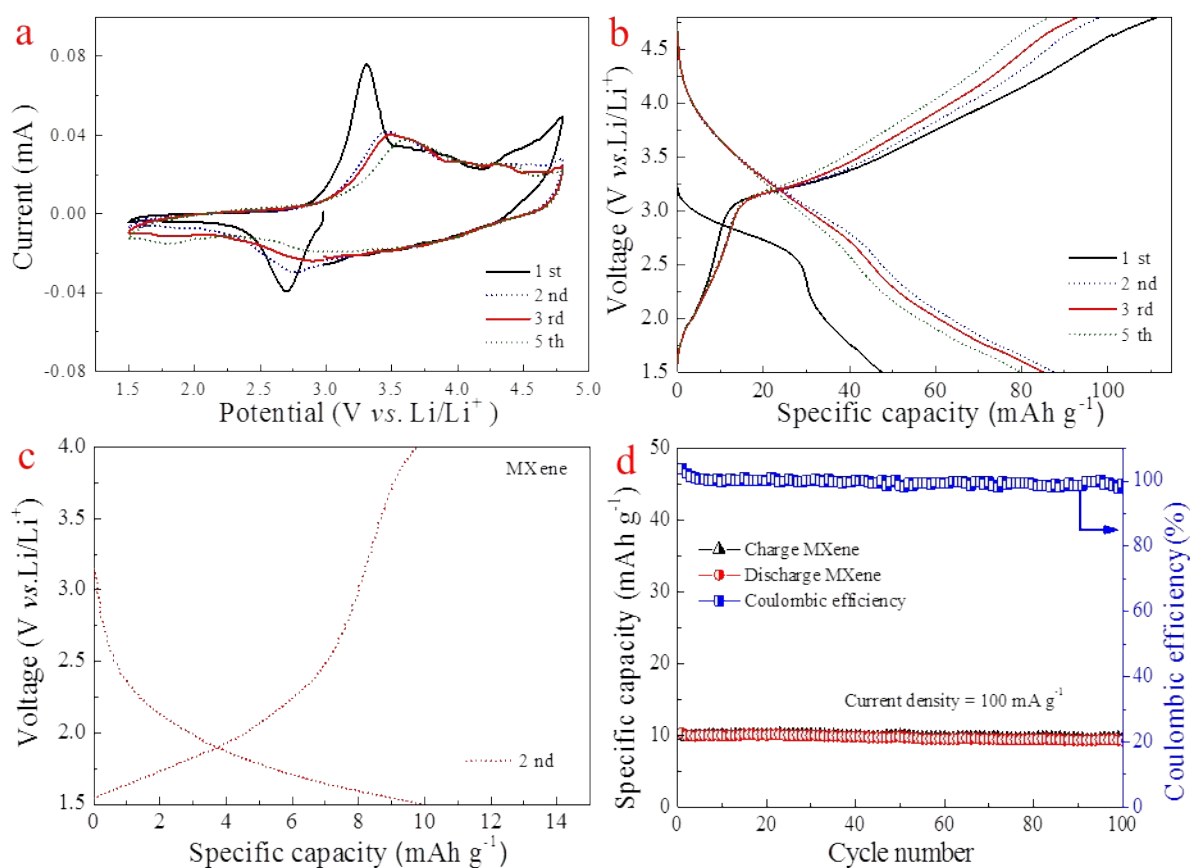
Fig. S12 (a) CV curves of the NMTO cathode at a scan rate of 0.2 mV s^{-1} over a voltage range of 1.5-4.8 V. (b) Charge-discharge profiles of the NMTO cathode at current density of 100 mA g^{-1}. (c) The discharge-charge curves of the pristine MXene over a voltage range of 1.5-4.0 V. (d) The cycle performances of the pristine MXene over a voltage range of 1.5-4.0 V at current density of 100 mA g^{-1}.
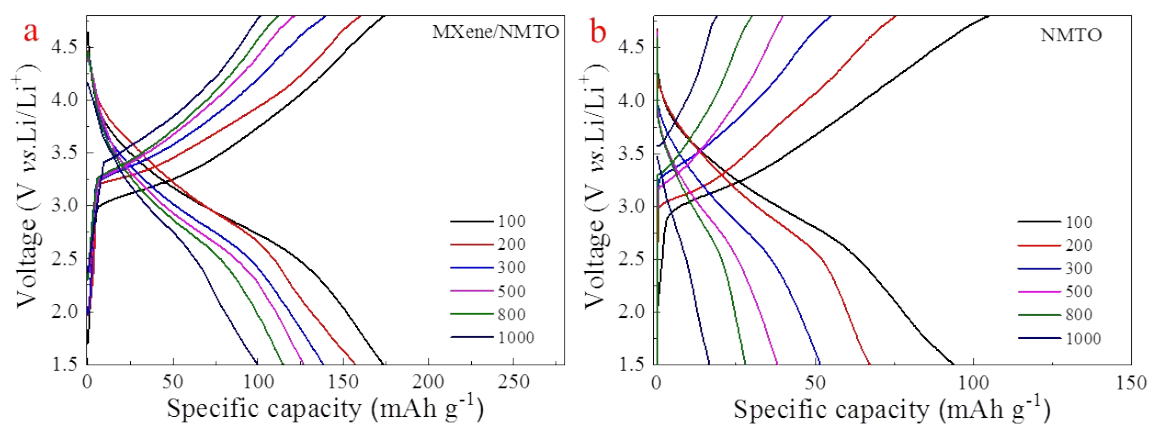
Fig. S13 The second discharge/charge profiles of MXene/NMTO (a) and NMTO (b) over a

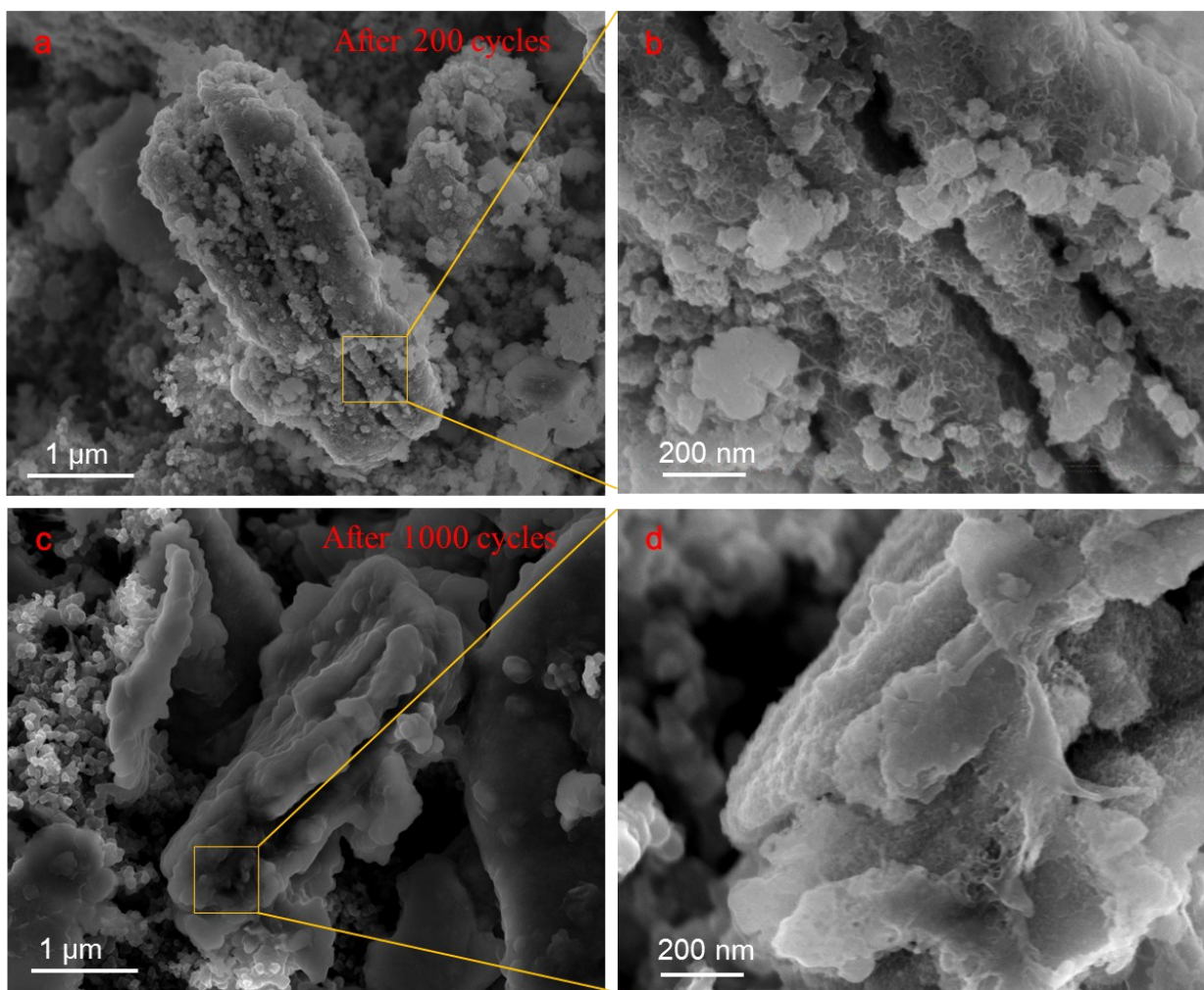voltage range of 1.5-4.8 V at current density of 100-1000 mA g⁻¹.

Fig. S14 SEM images of the MXene/NMTO sample after 200 cycles at current density of 5000

mA g^{-1} for the anode (a) and its local high magnification image (b). The SEM images of the

MXene/NMTO sample after 1000 cycles at current density of 5000 mA g^{-1} for the anode (c) and

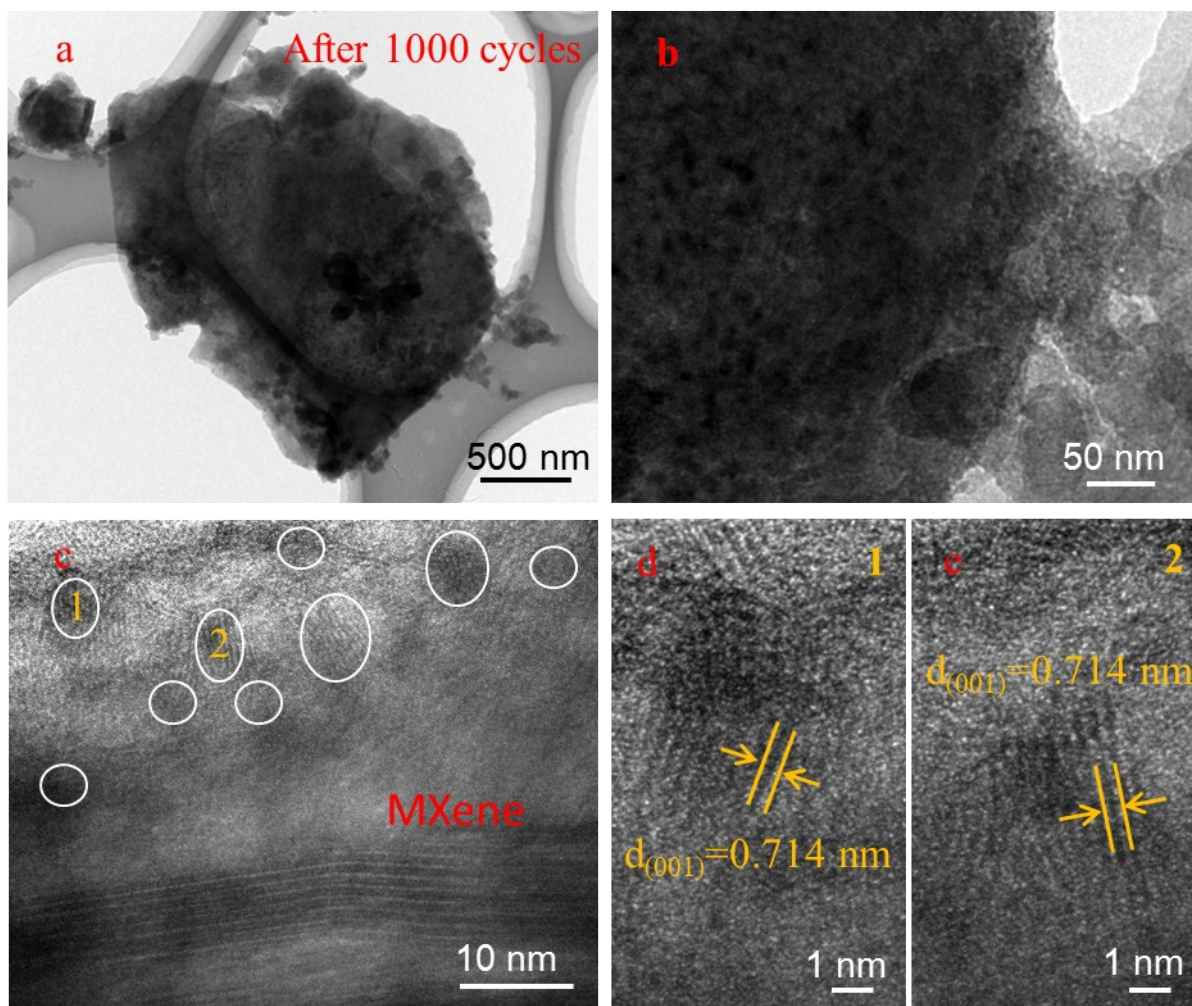its local high magnification image (d).

Fig. S15 Microstructures of MXene/NMTO sample after 1000 cycles at current density of 5000 mA g^{-1} for the anode. (a) TEM image, (b) local high magnification TEM image and (c) HRTEM image. (d) and (e) the corresponding high magnification images of the positions 1 and 2 in (c), respectively.